ISSN 0915-633X

NATIONAL INSTITUTE FOR FUSION SCIENCE

Three-dimensional MHD Equilibrium in the Presence of Bootstrap Current for Large Helical Device (LHD)

K. Watanabe, N. Nakajima, M. Okamoto, Y. Nakamura
and M. Wakatani

(Received – Feb. 12, 1992)

NIFS-139 Mar. 1992

RESEARCH REPORT
NIFS Series

NAGOYA, JAPAN

Three-dimensional MHD Equilibrium in the Presence of Bootstrap Current for Large Helical Device(LHD)

K.WATANABE, N.NAKAJIMA[+], M.OKAMOTO[+], Y.NAKAMURA[++], M.WAKATANI[++]

Nuclear Engineering Department, Faculty of Engineering, Kyoto University, Sakyo-ku, Kyoto 606, Japan

National Institute for Fusion Science, Nagoya 464-01, Japan[+]

Plasma Physics Laboratory, Kyoto University, Gokasho, Uji, Kyoto 611, Japan[++]

ABSTRACT

Three-dimensional MHD equilibria including the bootstrap current self-consistently are studied for the Large Helical Device(LHD). Magnitude of the bootstrap current is sensitive to the magnetic axis position or Shafranov shift in LHD, which is proportional to the plasma pressure and inversely proportional to the rotational transform. Since the bootstrap current enhances the rotational transform and reduces Shafranov shift, the self-consistent MHD equilibrium is crucial to estimate the bootstrap current. Total bootstrap current easily exceeds 100kA for LHD plasmas with $\langle\beta\rangle \gtrsim 1\%$ under the assumption that both electrons and ions belong to the rare-collisional $1/\nu$ regime in the whole plasma region, where $\langle\beta\rangle$ is a volume averaged beta value. Effects of the vertical field, the quadrupole field and the pressure profile on the bootstrap current are also investigated.

KEYWORDS : bootstrap current, three-dimensional MHD equilibrium, stellarator, heliotron, torsatron, Large Helical Device(LHD)

1. INTRODUCTION

It is believed that currentless plasmas are always confined in stellarators without the ohmic heating. However, the neoclassical theory of stellarators predicts the existence of the bootstrap current particularly for rare-collisional plasmas[1]. In several stellarators such as ATF[2] and WVII-AS[3] the bootstrap current was already measured and it agrees reasonably with the theoretical estimation based on the neoclassical theory. It should be noted that the maximum bootstrap current in ATF and WVII-AS are several kA. Its effect on the confinement properties is negligible in ATF; however, in WVII-AS, the small change of the rotational transform sometimes produces the low order resonance satisfying $\iota = n/m$ and destroys the flux surfaces, which degrades the energy confinement, where ι is a rotational transform, and m and n are the poloidal and toroidal mode numbers, respectively. This situation comes from the shear-less configuration in WVII-AS.

Recently Large Helical Device(LHD)[4,5] was designed to study confinement properties of rare-collisional plasmas in heliotron/torsatron type configuration. Since the LHD configuration is similar to ATF, the effect of the bootstrap current on the confinement may not be serious compared to the shear-less configuration. A simple way to calculate the bootstrap current in stellarators is the application of the result given by Shaing and Callen[1] to vacuum magnetic configurations. Plasma parameters and radial profiles of density, n, and electron and ion temperatures, T_e and T_i, are evaluated by using a stellarator transport code. When the vacuum magnetic field $B(\psi,\ \theta_B,\ \zeta_B)$ in the Boozer coordinates[6] and $n(\psi)$, $T_e(\psi)$, $T_i(\psi)$ are given, the bootstrap current can be evaluated. This type of analysis was already given for LHD[7]. For this case the bootstrap current, I_{bs}, becomes fairly large and $I_{bs} \gtrsim 200$kA for $\langle\beta\rangle \sim (1-2)\%$, where $\langle\beta\rangle$ is a volume averaged beta. It is natural to consider that this large bootstrap current affects the MHD stability and the transport phenomena. Before approaching these subjects we need the three-dimensional MHD equilibrium with the bootstrap current self-consistently. We em-

ploy the stellarator equilibrium code, the VMEC code[8,9], which is useful for studying the three-dimensional MHD equilibrium with the net plasma current. This code was already applied to study the bootstrap current of ATF[10].

The bootstrap current in the non-axisymmetric system was calculated in terms of the geometric factor G_{bs} for the $1/\nu$ collisional regime by Shaing and Callen[1] and for the plateau collisional regime by Shaing, Hirshman and Callen[11]. The bootstrap current can be written in the same form through the $1/\nu$, plateau and Pfirsch-Schlüter collisional regime[12]:

$$\langle J_{bs}B\rangle = -G_{bs}(L_{31}\frac{\mathrm{d}P}{\mathrm{d}\psi} + L^e_{32}n_e\frac{\mathrm{d}T_e}{\mathrm{d}\psi} + L^i_{32}n_i\frac{\mathrm{d}T_i}{\mathrm{d}\psi}), \tag{1}$$

where

$$\begin{aligned} L_{31} &= [\mu_{e1}(l^{ee}_{22}+\mu_{e3}) - \mu_{e2}(l^{ee}_{12}+\mu_{e2})]/D, \\ L^e_{32} &= (\mu_{e3}l^{ee}_{12} - \mu_{e2}l^{ee}_{22})/D, \\ L^i_{32} &= -L_{31}\mu_{i2}l^{ii}_{22}/[\mu_{i1}(l^{ii}_{22}+\mu_{i3}) - \mu^2_{i2}], \\ D &= (l^{ee}_{11}+\mu_{e1})(l^{ee}_{22}+\mu_{e3}) - (l^{ee}_{12}+\mu_{e2})^2. \end{aligned} \tag{2}$$

Here J_{bs} is the bootstrap current density, B is the magnitude of magnetic field, $\langle\ \rangle$ means the flux surface average(see Eq.(17)), n_e, n_i, T_e and T_i are the electron and ion density, the electron and ion temperature, respectively. P is the total pressure, $P = n_eT_e + n_iT_i$. $\psi \equiv \Phi_T/2\pi$, where Φ_T is the toroidal flux. An expression to calculate G_{bs} in the $1/\nu$ regime is described in Section 2. l^{ab}_{ij} are the friction coefficients between species a and b. By neglecting terms of $O(m_e/m_i)$, $l^{ee}_{11} = Z$, $l^{ee}_{12} = \frac{3}{2}Z$, $l^{ee}_{22} = \sqrt{2} + \frac{13}{4}Z$, and $l^{ee}_{22} = \sqrt{2}$. Here Z is the effective ionic charge number. We assume $Z = 1$ in this paper. μ_{aj} denote the viscosity coefficients. The expression (1) giving the bootstrap current is valid in the case that electrons and ions are in the same collisional regime. It is shown in Ref.[12] that the neoclassical current driven directly by the radial electric field, which does not exist in the axisymmetric systems, exists in the non-axisymmetric devices if electrons

and ions are in different collisional regimes. However, in this paper we restrict ourselves to the case that both electrons and ions are in the $1/\nu$ regime. In the rare-collisional $1/\nu$ regime, viscosity coefficients are expressed as[10,12]

$$\begin{aligned}
\mu_{a1} &= \frac{f_t}{f_c}\{\sqrt{2} - \ln(1+\sqrt{2}) + Z\delta_{ae}\}, \\
\mu_{a2} &= \frac{f_t}{f_c}\{2\sqrt{2} - \frac{5}{2}\ln(1+\sqrt{2}) + \frac{3}{2}Z\delta_{ae}\}, \\
\mu_{a3} &= \frac{f_t}{f_c}\{\frac{39}{8}\sqrt{2} - \frac{25}{4}\ln(1+\sqrt{2}) + \frac{13}{4}Z\delta_{ae}\},
\end{aligned} \tag{3}$$

where f_c is the fraction of untrapped particles and $f_t = 1 - f_c$. Here terms of $O(\sqrt{m_e/m_i})$ are neglected. When f_t/f_c is small, L_{31}, L_{32}^e and L_{32}^i are reduced to[1]

$$L_{31} = 1.63\frac{f_t}{f_c},\ L_{32}^e = -1.23\frac{f_t}{f_c},\ L_{32}^i = -1.91\frac{f_t}{f_c}. \tag{4}$$

Since $\vec{J}_{bs} = \langle J_{bs}B\rangle\vec{B}/\langle B^2\rangle$ is the bootstrap current density, the bootstrap current inside the flux surface, $I_T^{BSC}(\psi)$, is given by

$$\begin{aligned}
I_T^{BSC}(\psi) &= \frac{1}{2\pi}\int \sqrt{g_B}\mathrm{d}\psi\mathrm{d}\theta_B\mathrm{d}\zeta_B(\vec{J}_{bs}\cdot\nabla\zeta_B) \\
&= 2\pi\int \mathrm{d}\psi\frac{\langle J_{bs}B\rangle}{\langle B^2\rangle},
\end{aligned} \tag{5}$$

in the Boozer coordinates (ψ, θ_B, ζ_B), where $\sqrt{g_B} = (\nabla\psi\times\nabla\theta_B\cdot\nabla\zeta_B)^{-1}$.

Our approach to obtain the self-consistent three-dimensional MHD equilibrium with the bootstrap current is the following. First, the geometric factor G_{bs} is calculated for the three-dimensional currentless MHD equilibrium of LHD with a pressure profile $P(\psi)$. Here $n(\psi)$, $T_e(\psi)$ and $T_i(\psi)$ satisfying $P(\psi) = n(\psi)(T_e(\psi) + T_i(\psi))$ are specified to calculate $I_T^{BSC}(\psi)^{(1)}$. Next the three-dimensional MHD equilibrium including $I_T^{BSC}(\psi)^{(1)}$ is obtained by using the VMEC code. Now $B(\psi,\ \theta_B,\ \zeta_B)^{(1)}$ for the MHD equilibrium including the initial guess of the bootstrap current $I_T^{BSC}(\psi)^{(1)}$ is given, which is different from that for the currentless MHD equilibrium, $B(\psi,\ \theta_B,\ \zeta_B)^{(0)}$. With use of $B(\psi,\ \theta_B,\ \zeta_B)^{(1)}$, G_{bs} and $I_T^{BSC}(\psi)^{(2)}$ are calculated again. It is natural that $I_T^{BSC}(\psi)^{(2)} \neq I_T^{BSC}(\psi)^{(1)}$.

Then the VMEC code gives $B(\psi,\ \theta_B,\ \zeta_B)^{(2)}$ by using $I_T^{BSC}(\psi)^{(2)}$, and $I_T^{BSC}(\psi)^{(3)}$ is evaluated here. By iterating the above procedure N times,

$$|\frac{I_T^{BSC}(\psi_{Edge})^{(N+1)} - I_T^{BSC}(\psi_{Edge})^{(N)}}{I_T^{BSC}(\psi_{Edge})^{(N+1)}}| \leq 2 \times 10^{-2}$$

will be achieved. Here ψ_{Edge} denotes the boundary flux surface and $I_T^{BSC}(\psi_{Edge})$ corresponds to the total bootstrap current. For the LHD case with $\beta_0 < 5\%$, $N \simeq 5$ is sufficient to satisfy this criterion. When β_0 is increased more than 5%, the convergence becomes worse.

This paper is organized in the following way. In Section 2 numerical procedures to obtain the self-consistent three-dimensional MHD equilibrium with the bootstrap current is described briefly. In Section 3 properties of the geometric factor of LHD are studied by changing the vertical field and the quadrupole field. In Section 4 characteristics of the self-consistent three-dimensional MHD equilibrium with the bootstrap current in LHD are described. Particularly our interest is in dependency of the total bootstrap current on the beta value and in the change of the rotational transform due to the bootstrap current. In Section 5 results are discussed and future directions of our study are given.

2. NUMERICAL METHOD FOR THREE-DIMENSIONAL MHD EQUILIBRIUM WITH BOOTSTRAP CURRENT

For calculating the three-dimensional MHD equilibrium with net toroidal current such as the bootstrap current, we use the VMEC code. In the coordinates $(\psi,\ \theta,\ \zeta)$ of the VMEC code, the magnetic field $\vec{B}$ is expressed in the two ways[8],

$$\vec{B} = \nabla\psi \times \nabla(\theta - \iota\zeta - \lambda), \tag{6}$$

and

$$\vec{B} = B_\theta \nabla\theta + B_\zeta \nabla\zeta + B_\psi \nabla\psi, \tag{7}$$

where θ and ζ are the poloidal and toroidal angles, respectively. ι is the rotational transform, $\iota = \chi'$. Here $\chi \equiv \Phi_P/2\pi$, where Φ_P is the poloidal flux and the prime denotes the derivative with respect to ψ. λ and B_ψ are periodic functions with respect to θ and ζ. Then the current density, $\vec{J}$, and the total toroidal current inside flux surface, $I_T(\psi)$, are given by

$$\vec{J} = \frac{\partial B_\theta}{\partial \psi}\nabla\psi \times \nabla\theta + \frac{\partial B_\zeta}{\partial \psi}\nabla\zeta \times \nabla\psi + \nabla B_\psi \times \nabla\psi, \tag{8}$$

and

$$I_T(\psi) = \frac{1}{2\pi}\int \mathrm{d}\theta \mathrm{d}\zeta B_\theta. \tag{9}$$

Also the plasma pressure P is given as a function of ψ. Substituting $I_T^{BSC}(\psi)$ given by Eq.(5) into $I_T(\psi)$ in Eq.(9) gives the MHD equilibrium with the bootstrap current. Here geometric factor G_{bs} in Eq.(1) is calculated from the magnetic field of the finite beta equilibrium obtained by the VMEC code. As discussed in Section 1 a self-consistent MHD equilibrium solution with the bootstrap current is obtained by calculating the bootstrap current and the finite beta equilibrium including the net toroidal current iteratively.

Now we give an expression of G_{bs} and a numerical procedure to calculate it. It is more convenient to calculate G_{bs} in the Boozer coordinates $B(\psi,\ \theta_B,\ \zeta_B)$ than in the VMEC coordinates $B(\psi,\ \theta,\ \zeta)$ given by Eqs.(6) and (7). We develop a subroutine to construct the Boozer coordinates from the finite beta magnetic field including the effect of $I_T^{BSC}(\psi)$ given by the VMEC code.

In the Boozer coordinates $(\psi,\ \theta_B,\ \zeta_B)$, the magnetic field $\vec{B}$ and its Jacobian $\sqrt{g_B}$ are represented as[6]

$$\vec{B} = \nabla\psi \times \nabla\theta_B + \iota\nabla\zeta_B \times \nabla\psi, \tag{10}$$

$$\vec{B} = I\nabla\theta_B + G\nabla\zeta_B + \tilde{\beta}\nabla\psi, \tag{11}$$

and

$$\sqrt{g_B} = (\nabla\psi \times \nabla\theta_B \cdot \nabla\zeta_B)^{-1} = \frac{G + I/q}{B^2}, \tag{12}$$

where θ_B and ζ_B are the poloidal and toroidal angles, respectively. $G \equiv I_P/2\pi$, $I \equiv I_T/2\pi$, where I_P is the total poloidal current outside the flux surface. $\tilde{\beta}$ is the periodic function with respect to θ_B and ζ_B. When

$$\frac{1}{B^2} = \frac{1}{B_0^2}\{1 + \sum_{(n,m)\neq(0,0)} \epsilon_{nm}(\psi)\exp[\mathrm{i}(n\theta_B - m\zeta_B)]\}, \tag{13}$$

is given, the geometric factor G_{bs} in the rare-collisional $1/\nu$ regime is expressed as[10]

$$\begin{aligned} G_{bs} &= \langle H_1\rangle + \frac{H_2}{2}\frac{I+qG}{B_0^2}\langle B^2\rangle \\ &- \frac{3}{4}\frac{q}{f_t}\frac{I+qG}{B_0^2}\langle B^2\rangle \int_0^1 \frac{\lambda W(\lambda)\mathrm{d}\lambda}{\langle(1-\lambda B/B_{max})^{1/2}\rangle}, \end{aligned} \tag{14}$$

where $\lambda \equiv \mu B_{max}/\frac{1}{2}m_j v^2$, $|v_\parallel|/v = (1-\lambda B/B_{max})^{1/2}$, $q = 1/\iota$ is a safety factor, and

$$\begin{aligned} W(\lambda) &= \sum_{(n,m)\neq(0,0)} \frac{nR+mS}{n-mq}\{-2\frac{\partial\alpha_{nm}}{\partial\lambda}\langle\frac{|v_\parallel|}{v}\exp[-\mathrm{i}(n\theta_B - m\zeta_B)]\rangle \\ &+ \frac{1}{f_c}\frac{\langle B^2\rangle}{B_{max}^2}\exp[\mathrm{i}(n\theta_{max} - m\zeta_{max})](\frac{3}{2}\alpha_{nm}(\lambda=1) + d_{nm}) \\ &+ \frac{1}{2q}\frac{nR+mS}{n-mq}[-2\frac{\partial\beta_{nm}}{\partial\lambda}\langle\frac{|v_\parallel|}{v}\exp[-\mathrm{i}(n\theta_B - m\zeta_B)]\rangle \\ &+ \frac{1}{f_c}\frac{\langle B^2\rangle}{B_{max}^2}\exp[\mathrm{i}(n\theta_{max} - m\zeta_{max})](\frac{3}{2}\beta_{nm}(\lambda=1) + e_{nm})]\}. \end{aligned} \tag{15}$$

Here

$$\begin{aligned} \alpha_{nm} &= \langle\langle\frac{B}{B_{max}}\frac{|v_\parallel|}{v}\exp[-\mathrm{i}(n\theta_B - m\zeta_B)]\rangle\rangle, \\ \beta_{nm} &= \langle\langle\frac{B}{B_{max}}\frac{|v_\parallel|}{v}(\frac{B_0^2}{B^2}-1)\exp[-\mathrm{i}(n\theta_B - m\zeta_B)]\rangle\rangle, \\ d_{nm} &= \langle\langle\frac{|v_\parallel|^3}{v^3}\exp[-\mathrm{i}(n\theta_B - m\zeta_B)]\rangle\rangle, \\ e_{nm} &= \langle\langle\frac{|v_\parallel|^3}{v^3}(\frac{B_0^2}{B^2}-1)\exp[-\mathrm{i}(n\theta_B - m\zeta_B)]\rangle\rangle, \\ \langle H_1\rangle &= \frac{q}{2}(G - \frac{I}{q}), \\ H_2 &= [\langle(\partial B/\partial\theta)^2\rangle - q^2\langle(\partial B/\partial\zeta)^2\rangle]/\langle(\partial B/\partial\theta + q\partial B/\partial\zeta)^2\rangle, \\ R &= \frac{1}{2q}(1-H_2), \end{aligned} \tag{16}$$

$$S = \frac{1}{2}(1+H_2).$$

In Eqs.(14)-(16), $\langle\ \rangle$ denotes the flux surface average defined by

$$\langle A\rangle \equiv \frac{\int \sqrt{g_B}\mathrm{d}\theta_B\mathrm{d}\zeta_B\ A}{\int \sqrt{g_B}\mathrm{d}\theta_B\mathrm{d}\zeta_B}, \tag{17}$$

and

$$\langle\langle A\rangle\rangle \equiv \frac{1}{4\pi^2}\int \mathrm{d}\theta_B\mathrm{d}\zeta_B\ A. \tag{18}$$

The fraction of the trapped particle is expressed as

$$f_t = \frac{3}{4}\frac{\langle B^2\rangle}{B_0^2}\int_0^1 \frac{\lambda\mathrm{d}\lambda}{\langle(1-\lambda B/B_{max})^{1/2}\rangle}. \tag{19}$$

In Eq.(15), $(\theta_{max},\ \zeta_{max})$ are the values of $(\theta_B,\ \zeta_B)$ at $B = B_{max}$, where B_{max} is $max|\vec{B}|$ on the chosen flux surface.

3. PROPERTIES OF GEOMETRIC FACTOR G_{bs} FOR LHD

First we study G_{bs} for the vacuum magnetic configurations of LHD. In this paper, we use the final design parameters of LHD[5]; $L = 2$, $M = 10$, $R_C = 3.9$m, $B_0 = 3$T and $\alpha = 0.1$, where L and M are the pole number and the toroidal pitch number of the helical coil, R_C is the major radius at the axis of the helical coil, B_0 is the magnitude of the magnetic field there and α is the pitch modulation parameter defined $\theta_{\mathrm{QT}} = (L/M)\phi_{\mathrm{QT}} + \alpha\sin[(L/M)\phi_{\mathrm{QT}}]$. Here θ_{QT} and ϕ_{QT} are the poloidal and toroidal angles in the quasi-toroidal coordinates. By controlling R_{ax}^V and B_Q with the vertical field and the quadrupole field, respectively, we study various configurations, where R_{ax}^V is the major radius of the vacuum magnetic axis and B_Q is the quadrupole field produced by the axisymetric poloidal coils which is added to the quadrupole field by the helical coil.

Figures 1(a) and (b) show poloidal cross sections of vacuum flux surfaces calculated by the VMEC code. The axis of the torus is located on the left hand side of the figures

in Fig.1. Flux surfaces in the upper and lower column correspond to cross sections at $M\zeta = 0°$ and $M\zeta = 180°$, respectively. Here ζ is the toroidal angle coordinate in the VMEC coordinates. The plasma boundary is defined at the outermost magnetic surface in the vacuum magnetic configuration, which is determined by the line tracing calculation. Figure 1(a) shows three cases of flux surface at $R_{ax}^V = 3.6$m(left), $R_{ax}^V = 3.75$m(middle) and $R_{ax}^V = 3.9$m(right). In these cases, $B_Q = 100\%$ is kept, which means that the quadrupole field produced by the helical coils are completely canceled by that by the axisymetric poloidal coils. In other words, the average cross section of the flux surface over the one field pitch length becomes circular. The magnetic configuration with $R_{ax}^V = 3.75$m and $B_Q = 100\%$ is referred as the 'standard configuration'. Figure 1(b) shows flux surfaces for various cases of B_Q ($B_Q = 0$, 100 and 200%) when R_{ax}^V is fixed at 3.75m. The cross section averaged over one field pitch length becomes vertically elongated for $B_Q = 0\%$ and horizontally elongated for $B_Q = 200\%$.

By considering that the bootstrap current in the rare-collisional $1/\nu$ regime is proportional to $(f_t/f_c)G_{bs}$ for the small f_t/f_c limit, we plot $(f_t/f_c)G_{bs}$ for various magnetic configurations of LHD. Figures 2(a) and (b) show the radial profile of $(f_t/f_c)G_{bs}$ when R_{ax}^V and B_Q are varied, respectively. Solid lines in Figs.2(a) and (b) indicate the standard configuration. In Fig.2(a), R_{ax}^V is changed from 3.6m to 4.05m with $B_Q = 100\%$. $(f_t/f_c)G_{bs}$ becomes large as R_{ax}^V changes from 3.6m to 3.825m, while it becomes small as R_{ax}^V is increased more than 3.9m. It should be noted that $(f_t/f_c)G_{bs}$ is significantly reduced for R_{ax}^V larger than 3.975m. It was already shown in Refs.[7,10] that the outward shift of the magnetic axis reduces $(f_t/f_c)G_{bs}$. Here it is remarkable that the large inward shift of magnetic axis also reduces $(f_t/f_c)G_{bs}$. In Fig.2(b), B_Q is changed from 0% to 200% with $R_{ax}^V = 3.75$m. Although the vertical elongation of the flux surface or $B_Q = 0\%$ reduces $(f_t/f_c)G_{bs}$ and the horizontal elongation or $B_Q = 200\%$ enhances it, the effect of B_Q on $(f_t/f_c)G_{bs}$ is not significant. It should be noted that $(f_t/f_c)G_{bs}$ depends on B_Q strongly for the case of the outward magnetic axis shift, while it depends on B_Q weakly

for the inward shift case[7]. Here $R_{ax}^V = 3.75$m belongs to the latter case.

4. BOOTSTRAP CURRENT OF FINITE BETA LHD PLASMAS

Here we assume that the collisionality of the whole plasma belongs to the $1/\nu$ regime and that the outermost flux surface boundary is fixed even for finite beta equilibria. Figures 3-6 show the properties of finite beta MHD equilibrium with the self-consistent bootstrap current in the standard configuration with $R_{ax}^V = 3.75$m and $B_Q = 100\%$. It's flux surfaces are shown in the middle column of Figs.1(a) and (b). The plasma parameters are assumed $n = n_0(1-\psi)$ and $T_i = T_e = T_0(1-\psi)$, where $n_0 = 0.5 \times 10^{20}\mathrm{m}^{-3}$ is fixed and T_0 is varied. This case corresponds to $\beta = \beta_0(1-\psi)^2$, and the volume averaged beta is given by $\langle\beta\rangle \sim \beta_0/3$. Here β_0 is changed from 0% to 4.47%. Figure 3 shows the total bootstrap current, I_{bs}, and Shafranov shift versus central beta value, β_0. Circles correspond to the MHD equilibrium with the self-consistent bootstrap current. In Fig.3(a) squares denote the bootstrap current estimated by using the currentless MHD equilibrium. Solid line denotes the bootstrap current estimated by using the geometric factor for the vacuum magnetic field. In Fig.3(b) squares denote the Shafranov shift of the currentless MHD equilibrium. Figures 4, 5 and 6 show the radial profile of rotational transform, $\hat{L}_{31}G_{bs}$ and G_{bs} normalized by $(G_{bs})_T$, which refers to G_{bs} of tokamaks and $(G_{bs})_T = I_P/2\pi\iota$, for various β_0. Left figures in Figs.4-6 correspond to the currentless MHD equilibrium and right ones to the MHD equilibrium including the bootstrap current self-consistently. From Eq.(1) the bootstrap current in the $1/\nu$ regime is also shown as

$$\langle J_{bs}B\rangle = -1.63\hat{L}_{31}G_{bs}P(\frac{n'}{n} + \alpha_1\frac{T_i'}{T} + \alpha_2\frac{T_e'}{T}). \tag{20}$$

Here we note that $1.63\hat{L}_{31}G_{bs} = L_{31}G_{bs}$ and $\hat{L}_{31}G_{bs} \to (f_t/f_c)G_{bs}$ in the limit of $f_t/f_c \to 0$. Though α_1 and α_2 depend on f_t/f_c, the magnitude of α_1 and α_2 is usually on the order of 10^{-1}. Thus it is considered that $\hat{L}_{31}G_{bs}$ determines the dominant geometrical

contribution to $\langle J_{bs}B\rangle$. Figure 3(a) shows that the total bootstrap current is about 230kA for the MHD equilibrium with $\beta = \beta_0(1-\psi)^2$ and $\beta_0 = 4.5\%$ including the bootstrap current self-consistently. However, this bootstrap current is as large as that estimated by using the currentless MHD equilibrium at $\beta_0 = 4.5\%$. We note that I_{bs} obtained from the currentless MHD equilibrium decreases as β_0 increases more than $\beta_0 = 3.5\%$. The increase of β_0 makes Shafranov shift of the magnetic axis significantly large in the currentless equilibrium as shown by squares in Fig.3(b). As similar to the dependency of the geometric factor on the vacuum magnetic configurations in Fig.2(a), the large Shafranov shift reduces $(f_t/f_c)G_{bs}$ substantially(see the left figure in Fig.5). Since the bootstrap current is determined by the competition with the increase of P and the decreases of $\hat{L}_{31}G_{bs}$ as seen in Eq.(20), I_{bs} estimated from the currentless MHD equilibrium has the maximum value at $\beta_0 \sim 3.5\%$.

Next we consider dependency of I_{bs} on β_0 for the MHD equilibrium including the bootstrap current self-consistently. For $\beta_0 \lesssim 4\%$, the self-consistent MHD equilibrium gives smaller I_{bs} than that obtained from the currentless MHD equilibrium. This is understandable by the following relation. The geometric factor depends on ι as

$$G_{bs} \propto \iota^{-1}. \tag{21}$$

As shown in Fig.4, the self-consistent MHD equilibrium has the larger ι in the whole plasma region than that of the currentless MHD equilibrium with the same $\beta(\psi)$, since the bootstrap current usually enhances the rotational transform. This increase of the rotational transform by the bootstrap current suppresses the Shafranov shift. Thus, for $\beta_0 \lesssim 4\%$, the self-consistent MHD equilibrium has smaller $\hat{L}_{31}G_{bs}$ and I_{bs} than the currentless MHD equilibrium.

Figure 6 shows that G_{bs} normalized by $(G_{bs})_T (= I_P/2\pi\iota)$ hardly changes for the MHD equilibrium including the bootstrap current, while $G_{bs}/(G_{bs})_T$ for the currentless MHD equilibrium decreases significantly for $\beta_0 \gtrsim 3\%$. From simplified relations $\Delta\iota_{bs} \sim c_1 I_{bs}$ and

$G_{bs} \sim c_2/\iota$, we have

$$I_{bs} \sim c_3 \beta G_{bs} \sim \frac{c_2 c_3 \beta}{\iota_0 + \Delta\iota_{bs}} \sim \frac{c_2 c_3 \beta}{\iota_0 + c_1 I_{bs}}, \tag{22}$$

where c_1, c_2 and c_3 are positive constant and $\Delta\iota_{bs}$ denotes the increment of the rotational transport due to the bootstrap current. Thus we obtain the relation between I_{bs} and β,

$$I_{bs} \sim \frac{\sqrt{\iota_0^2 + 4c_1 c_2 c_3 \beta} - \iota_0}{2c_1}. \tag{23}$$

This shows that I_{bs} for the MHD equilibrium including the self-consistent bootstrap current increases monotonously according to the increase of β as shown in Fig.3(a). Moreover Fig.3(a) shows that the bootstrap current estimated by using the vacuum magnetic field[7] is proportional to β_0 and becomes about twice as large as that estimated by using the MHD equilibrium including the bootstrap current self-consistently.

Figures 7 and 8 show the total bootstrap current and Shafranov shift for various pressure profiles, respectively. Left figures in Figs.7 and 8 show the results for the currentless MHD equilibrium. Right figures show the results for the MHD equilibrium including the self-consistent bootstrap current. Circles correspond to the pressure profile of $\langle\beta\rangle \sim \beta_0/3$, where $n = n_0(1-\psi)$ and $n_0 = 0.5 \times 10^{20}\mathrm{m}^{-3}$. Squares correspond to the pressure profile of $\langle\beta\rangle \sim 0.45\beta_0$, where $n = n_0(1-\psi^3)$ and $n_0 = 0.65 \times 10^{20}\mathrm{m}^{-3}$. Triangles correspond to the pressure profile of $\langle\beta\rangle \sim \beta_0/4$, where $n = n_0(1-\psi)^2$ and $n_0 = 1.5 \times 10^{20}\mathrm{m}^{-3}$. In all cases the temperature profile is fixed at $T_i = T_e = T_0(1-\psi)$, and T_0 is varied to change $\langle\beta\rangle$. For several peaked pressure profiles, I_{bs} obtained by assuming the currentless MHD equilibrium has the maximum value with respect to $\langle\beta\rangle$ or β_0. The currentless MHD equilibrium with the more peaked pressure profile has the lower $\langle\beta\rangle$ giving the maximum value of I_{bs}. This is understandable from the fact that the MHD equilibrium with the more peaked pressure profile has the larger Shafranov shift. The maximum values of I_{bs} are about 250kA which seems independent of the pressure profile. For the MHD equilibrium including the self-consistent bootstrap current, I_{bs} increases monotonously with the

increase of $\langle\beta\rangle$, as shown in Fig.3(a) and Fig.7 for various pressure profiles. However, the magnitude of I_{bs} depends on the pressure profile. Since $\hat{L}_{31}G_{bs}$ is large in the inner plasma region, the MHD equilibrium with the more peaked pressure profile has the larger I_{bs} for the same $\langle\beta\rangle$. In the case of $\langle\beta\rangle \sim 1\%$ in Fig.7, the MHD equilibrium with $\beta \propto (1-\psi)^3$ has I_{bs} about twice as large as I_{bs} in the case with $\beta \propto (1-\psi^3)(1-\psi)$. It was already shown in Ref.[7] that the magnitude of I_{bs} depends sensitively on the pressure profile. In particular, the hollow density profile significantly reduces I_{bs}. It is remarkable that the MHD equilibrium including the self-consistent bootstrap current has almost identical Shafranov shift for various pressure profiles. This is understandable from the fact that the enhancement of Shafranov shift is canceled by the reduction of Shafranov shift due to the large I_{bs} in the case of the peaked pressure profile.

Furthermore we investigated how the bootstrap current changes by controlling the vacuum magnetic axis position, R_{ax}^V, and the external quadrupole field, B_Q. Figures 9 and 10 show the dependency of the total bootstrap current and Shafranov shift on the vacuum magnetic axis position R_{ax}^V, respectively. Left figures in Figs.9 and 10 show the results for the currentless MHD equilibrium. Right figures show the results for the MHD equilibrium including the self-consistent bootstrap current. Circles correspond to $R_{ax}^V = 3.75$m(standard configuration). Squares correspond to $R_{ax}^V = 3.6$m and triangles to $R_{ax}^V = 3.9$m. Here the external quadrupole field is fixed at $B_Q = 100\%$. The currentless MHD equilibrium with the smaller R_{ax}^V has the larger maximum I_{bs} at the larger β_0. Since the currentless finite beta MHD equilibrium corresponding to the larger R_{ax}^V has the more external magnetic axis position, G_{bs} reduces significantly in this situation. This may explain the maximum I_{bs} appears at $\beta_0 \sim 2.3\%$ for $R_{ax}^V = 3.9$m instead of 3.5% for the standard configuration. For the MHD equilibrium including the self-consistent bootstrap current, I_{bs} becomes smaller when the vacuum magnetic axis shifts inward. I_{bs} for $R_{ax}^V = 3.6$m is about two thirds of I_{bs} for $R_{ax}^V = 3.9$m. From Fig.10, Shafranov shift becomes larger when the vacuum magnetic axis is shifted more inward. Figures 11 and 12

show the radial profile of (a) G_{bs} normalized by $(G_{bs})_T$ and (b) rotational transform for the configurations with $R_{ax}^V = 3.6$m and $R_{ax}^V = 3.9$m, respectively. Figure 11 corresponds to squares in the right figures of Figs.9 and 10. Figure 12 corresponds to triangles in the right figures of Figs.9 and 10. For $R_{ax}^V = 3.6$m, $G_{bs}/(G_{bs})_T$ increases slightly with the increase of β_0 as shown in Fig.11(a). On the contrary, for $R_{ax}^V = 3.9$m, $G_{bs}/(G_{bs})_T$ decreases slightly with the increase of β_0 as shown in Fig.12(a). Since $G_{bs}/(G_{bs})_T$ for $R_{ax}^V = 3.6$m is smaller than that for $R_{ax}^V = 3.9$m, it is expected that the configuration with the smaller R_{ax}^V has the smaller I_{bs}. This is consistent with the right figure in Fig.9. Moreover the configuration with the smaller R_{ax}^V has the smaller change of the rotational transform.

Figure 13 shows the dependency of (a) the total bootstrap current and (b) Shafranov shift on the quadrupole field. B_Q is changed from 0% to 200% with $R_{ax}^V = 3.75$m. We note that $B_Q = 100\%$ corresponds to the standard configuration. The plasma parameters are assumed $n = n_0(1-\psi)$ and $T_i = T_e = T_0(1-\psi)$ with $n_0 = 0.5 \times 10^{20}\mathrm{m}^{-3}$ and $T_0 = 5$keV, which give $\beta_0 = 2.23\%$. Circles correspond to the MHD equilibrium including the self-consistent bootstrap current and squares to the currentless MHD equilibrium. The bootstrap current becomes lower for the configuration with more vertically elongated flux surfaces. This result is the same as that already found for the vacuum magnetic configurations[7]. For the MHD equilibrium including the self-consistent bootstrap current, I_{bs} for $B_Q = 0\%$ is about a half of that for $B_Q = 200\%$. As for Shafranov shift, the MHD equilibrium with the larger B_Q has the larger Shafranov shift. As similar to I_{bs}, Shafranov shift for the MHD equilibrium including the self-consistent bootstrap current depends more weakly on B_Q than that for the currentless MHD equilibrium.

5. CONCLUDING REMARKS

We studied the properties of the three-dimensional MHD equilibrium by including

the bootstrap current self-consistently for the Large Helical Device(LHD). According to the neoclassical transport theory the bootstrap current density is proportional to the geometric factor G_{bs} and to the density and temperature gradients. The geometric factor G_{bs} in the rare-collisional $1/\nu$ regime is calculated from the magnetic field of the three-dimensional finite beta MHD equilibrium obtained by the VMEC code. A self-consistent equilibrium with the bootstrap current is obtained by calculating the bootstrap current density as a function of flux surface and the finite beta equilibrium with the net toroidal plasma current iteratively. After this numerical procedure is converged, we calculate the total bootstrap current. When the pressure profile is $P = P_0(1-\psi)^2$ and the collisionality of the whole plasma is in the $1/\nu$ regime, the total bootstrap current, I_{bs} of the standard configuration with $R_{ax}^V = 3.75$m and $B_Q = 100\%$, is about 230kA for the self-consistent MHD equilibrium with $\beta_0 \sim 4.5\%$. This current is comparable to the bootstrap current estimated from the currentless MHD equilibrium. Usually the former self-consistent bootstrap current is smaller than the latter estimation of I_{bs} for the low beta plasma. I_{bs} for the currentless MHD equilibrium has maximum value at $\beta_0 = \beta_{max}$ and I_{bs} decreases as β_0 is increased above β_{max}. On the other hand, I_{bs} for the MHD equilibrium with the self-consistent bootstrap current increases monotonously with the increase of β.

In the LHD configuration the bootstrap current flows to enhance the rotational transform in the whole plasma column. Since Shafranov shift is inversely proportional to the rotational transform, the bootstrap current has a tendency to suppress the Shafranov shift. Thus Shafranov shift becomes smaller for the MHD equilibrium with the self-consistent bootstrap current than that for the currentless MHD equilibrium. This reduction of Shafranov shift may affect the stability beta limit significantly[13], since the magnetic well produced by Shafranov shift is reduced.

We calculated I_{bs} for the MHD equilibrium with the self-consistent bootstrap current for various pressure profiles. When the volume averaged beta value, $\langle\beta\rangle$, is kept constant, the MHD equilibrium with the more peaked pressure profile gives the larger I_{bs}. In the

case of $\langle\beta\rangle \sim 1\%$, the MHD equilibrium with the peaked pressure of $\beta \propto (1-\psi)^3$ has I_{bs} about twice as large as that with the flat pressure of $\beta \propto (1-\psi^3)(1-\psi)$.

Furthermore we calculated the bootstrap current by controlling the vacuum magnetic axis position R_{ax}^V and the external quadrupole field produced by the axisymmetric poloidal coils B_Q. Under the assumption of the currentless MHD equilibrium, the maximum I_{bs} with respect to β_0 decreases when R_{ax}^V becomes large. On the contrary, the MHD equilibrium with the self-consistent bootstrap current gives monotonously increasing I_{bs} with the increase of β, and I_{bs} decreases when R_{ax}^V becomes small. As for the effect of B_Q on I_{bs}, the lower I_{bs} is obtained for the configuration with the more vertically elongated flux surfaces. However, I_{bs} for the MHD equilibrium with the self-consistent bootstrap current depends on B_Q more weakly than that estimated from the currentless MHD equilibrium. It should be noted that the self-consistent I_{bs}decreases for the configuration with the smaller R_{ax}^V and the more vertically elongated flux surfaces.

In this paper we assumed that the collisionality of the whole plasma column belongs to the $1/\nu$ regime for both electrons and ions. However, this assumption is ideal and the collisionality of the edge plasma or of the plasma near the magnetic axis is likely to be in the plateau regime. It should be noted that the bootstrap current in the plateau regime is much smaller than that in the $1/\nu$ regime[7,11]. Further the geometric factor which we have used is valid in the limit of $1/\nu$ regime. The geometric factor should depend on the collisionarity decreasing in the transition regime from the $1/\nu$ regime towards the plateau regime. Thus I_{bs} shown in Section 4 might be overestimated if the plateau regime exists in the plasma column. Moreover, it is shown that the parallel current proportional to the radial electric field can be generated when electrons and ions are in different collisional regimes (for instance electrons are in the $1/\nu$ regime and ions in the plateau regime as obtained in the ECH plasma)[12]. This current, which does not exist in the axisymmetric system, tends to cancel the conventional pressure driven neoclassical bootstrap current. The estimation of the bootstrap current for a plasma in which electrons and ions are in

different collisional regimes will be published in another paper.

We also studied the bootstrap current in the finite beta plasmas under the assumption that the outermost flux surface is fixed. This makes the geometric factor G_{bs} in the outer edge plasma region hardly changeable even in the finite beta plasma except the contribution from the rotational transform ι. It is expected that the free boundary MHD equilibrium with $\langle\beta\rangle \gtrsim 1\%$ may have a considerably different outermost flux surface comparing to the fixed boundary case[10,14]. This effect may be important for the bootstrap current in the edge plasma region since the deformation of outermost surface due to the free boundary effect changes the geometric factor G_{bs} there.

The bootstrap current may significantly affect the MHD stability and the particle and energy confinement of LHD particularly for the high beta plasma with $\langle\beta\rangle \gtrsim (1-2)\%$, since the bootstrap current changes the magnetic shear and Shafranov shift substantially. These are our future study subjects.

ACKNOWLEDGEMENTS

The author K.W acknowledge National Institute for Fusion Science for giving a chance to stay and study the bootstrap current in LHD as a visiting graduate student from Kyoto University. We acknowledge Dr S. P. Hirshman for permitting to use the VMEC code in Kyoto University and Dr. K. C. Shaing for valuable discussions about the bootstrap current theory of stellalator.

REFERENCES

[1] SHAING, K.C., CALLEN, J.D., Phys. Fluids **26** (1983) 3315.

[2] MURAKAMI, M., CARRERAS, B.A., BAYLOR, L.R., BELL, G.L., BIGELOW, T.S., ENGLAND, A.C., GLOWIENKA, J.C., HOWE, H.C., JERNIGAN, T.C., LEE, D.K., LYNCH, V.E., MA, C.H., RASMUSSEN, D.A., TOLLIVER, J.S., WADE, M.R., WILGEN, J.B., WING, W.R., Phys. Rev. Lett. **66** (1991) 707.

[3] RENNER, H., GASPARINO, U., MAASSBERG, H., KÜHNER, G., RINGLER, H., SARDEI, F., WELLER, A., W7AS TEAM, NBI GROUP, PELLET INJECTION GROUP, ECH TEAM, in Plasma Physics and Controlled Nuclear Fusion Research 1990 (Proc. 13th Int. Conf. Washington DC, 1990), Vol.2, IAEA, Vienna (1991) 439.

[4] IIYOSHI, A., FUJIWARA, M., MOTOJIMA, O., OHYABU, N., YAMAZAKI, K., Fusion Technology **17** (1990) 169.

[5] YAMAZAKI, K., KANEKO, H., TANIGUCHI, Y., MOTOJIMA, O., LHD DESIGN GROUP, Status of LHD Control System Design, National Institute for Fusion Science Report, NIFS-122, Dec. 1991.

[6] BOOZER, A.H., Phys. Fluids **23** (1980) 904.

[7] NAKAJIMA, N., OKAMOTO, M., TODOROKI, J., NAKAMURA, Y., WAKATANI, M., Nucl. Fusion **29** (1989) 605.

[8] HIRSHMAN, S.P., Phys. Fluids **26** (1983) 3553.

[9] HIRSHMAN, S.P., VAN RIJ, W.I., MERKEL, P., Comp. Phys. Commun. **43** (1986) 143.

[10] SHAING, K.C., CARRERAS, B.A., DOMINGUEZ, N., LYNCH, V.E., TOLLIVER, J.S., Phys. Fluids **B1** (1989) 1663.

[11] SHAING, K.C., HIRSHMAN, S.P., CALLEN, J.D., Phys. Fluids **29** (1986) 521.

[12] NAKAJIMA, N., OKAMOTO, M., to be published in J. Phys. Soc. Jpn. **61** No.3 (1992).

[13] NAKAMURA, Y., WAKATANI, M., LEBOEUF, J.-N., CARRERAS, B.A., DOMINGUEZ, N., HOLMES, J.A., LYNCH, V.E., PAINTER, S.L., Fusion Technology **19** (1991) 217.

[14] MERKEL, P., J. Comp. Phys. **66** (1986) 83.

FIGURE CAPTIONS

Fig.1 Vacuum magnetic surface of LHD calculated by the VMEC code. (a) The magnetic axis position is controlled by vertical field for $B_Q = 100\%$; $R_{ax}^V = 3.6$m(left), $R_{ax}^V = 3.75$m(middle) and $R_{ax}^V = 3.9$m(right). (b) The quadrupole field is controlled for $R_{ax}^V = 3.75$m; $B_Q = 0\%$(left), $B_Q = 100\%$(middle) and $B_Q = 200\%$(right). Here $B_Q = 100\%$ means that the quadrupole field produced by the axisymetric poloidal coils is equal to that by the helical coil.

Fig.2 Radial profiles of $(f_t/f_c)G_{bs}$ for various vacuum magnetic configurations. $\bar{r}$(m) denotes the minor radius of the averaged flux surface. Solid lines correspond to the standard magnetic configuration with $R_{ax}^V = 3.75$m and $B_Q = 100\%$. (a) R_{ax}^V is changed from 3.6m to 4.05m with $B_Q = 100\%$. (b) B_Q is changed from 0% to 200% with $R_{ax}^V = 3.75$m.

Fig.3 (a) Total bootstrap current and (b) Shafranov shift for the standard configuration versus central beta value, β_0. Circles correspond to the MHD equilibrium with the self-consistent bootstrap current and squares to the currentless MHD equilibrium, respectively. The solid line denotes the bootstrap current estimated by using the geometric factor for the vacuum magnetic configuration. The density and temperature profiles are $n = n_0(1-\psi)$ and $T_i = T_e = T_0(1-\psi)$, where $n_0 = 0.5 \times 10^{20}\mathrm{m}^{-3}$ and T_0 is varied. For these profiles $\langle\beta\rangle \sim \beta_0/3$.

Fig.4 Radial profile of rotational transform for the various β_0. β_0 is changed from 0% to 4.47%. Left figure denotes the rotational transform for the currentless MHD equilibrium corresponding to the squares in Fig.3. Right figure denotes the rotational transform for the MHD equilibrium with the self-consistent bootstrap current corresponding to the circles in Fig.3.

Fig.5 Radial profile of $\hat{L}_{31}G_{bs}$ for various β_0, where $\hat{L}_{31}G_{bs} = L_{31}G_{bs}/1.63$ converges to $(f_t/f_c)G_{bs}$ in the limit of small (f_t/f_c). Others are the same as in Fig.4.

Fig.6 Radial profile of G_{bs} normalized by $(G_{bs})_T$ for various β_0. $(G_{bs})_T = I_P/2\pi\iota$ corresponds to G_{bs} of tokamak. Others are the same as in Fig.4.

Fig.7 Dependency of total bootstrap current on the pressure profile. Left figure shows total bootstrap current evaluated from the currentless MHD equilibrium. Right figure shows total bootstrap current for the MHD equilibrium with the self-consistent bootstrap current. Circles correspond to $\langle\beta\rangle \sim \beta_0/3$, where $n = n_0(1-\psi)$ and $n_0 = 0.5\times10^{20}\mathrm{m}^{-3}$. Squares correspond to $\langle\beta\rangle \sim 0.45\beta_0$, where $n = n_0(1-\psi^3)$ and $n_0 = 0.65\times10^{20}\mathrm{m}^{-3}$. Triangles correspond to $\langle\beta\rangle \sim \beta_0/4$, where $n = n_0(1-\psi)^2$ and $n_0 = 1.5\times10^{20}\mathrm{m}^{-3}$. Temperature profile is fixed at $T_i = T_e = T_0(1-\psi)$ and T_0 is varied to change $\langle\beta\rangle$.

Fig.8 Dependency of Shafranov shift on the pressure profile. Others are the same as in Fig.7.

Fig.9 Total bootstrap current for the magnetic configurations with various vacuum magnetic axis positions versus β_0. Left figure shows total bootstrap current evaluated from the currentless MHD equilibrium. Right figure shows total bootstrap current for the MHD equilibrium with the self-consistent bootstrap current. Circle correspond to $R_{ax}^V = 3.75$m(standard configuration), which are the same as in Fig.3(a). Squares correspond to $R_{ax}^V = 3.6$m. Triangles correspond to $R_{ax}^V = 3.9$m. The quadrupole field by the axisymetric poloidal coils is fixed at $B_Q = 100\%$. The density and temperature profile are $n = n_0(1-\psi)$ and $T_i = T_e = T_0(1-\psi)$, respectively, where $n_0 = 0.5\times10^{20}\mathrm{m}^{-3}$ and T_0 is varied to change $\langle\beta\rangle$. Here $\langle\beta\rangle \sim \beta_0/3$.

Fig.10 Shafranov shift for the magnetic configurations with various vacuum magnetic axis positions versus β_0. Others are the same as in Fig.9.

Fig.11 Radial profile of (a) $G_{bs}/(G_{bs})_T$ and (b) rotational transform for various β_0. β_0 is changed from 0% to 4.47%. These results correspond to squares in right figures of Figs.9 and 10 for the MHD equilibrium with $R_{ax}^V = 3.6$m including the self-consistent bootstrap current.

Fig.12 Radial profile of (a) $G_{bs}/(G_{bs})_T$ and (b) rotational transform for various β_0. β_0 is changed from 0% to 4.47%. These results correspond to triangles in right figures of Figs.9 and 10 for the MHD equilibrium with $R_{ax}^V = 3.9$m including the self-consistent bootstrap current.

Fig.13 (a) Total bootstrap current and (b) Shafranov shift for various values of quadrupole field. B_Q is changed from 0% to 200%. $R_{ax}^V = 3.75$m is fixed. Here $B_Q = 100\%$ corresponds to the standard configuration. Circles correspond to the MHD equilibrium with the self-consistent bootstrap current and squares to the currentless MHD equilibrium. The density and temperature profiles are $n = n_0(1-\psi)$ and $T_i = T_e = T_0(1-\psi)$, respectively, where $n_0 = 0.5 \times 10^{20}\mathrm{m}^{-3}$, and $T_0 = 5$keV which give $\beta_0 = 2.23\%$ and $\langle\beta\rangle = 0.74\%$.

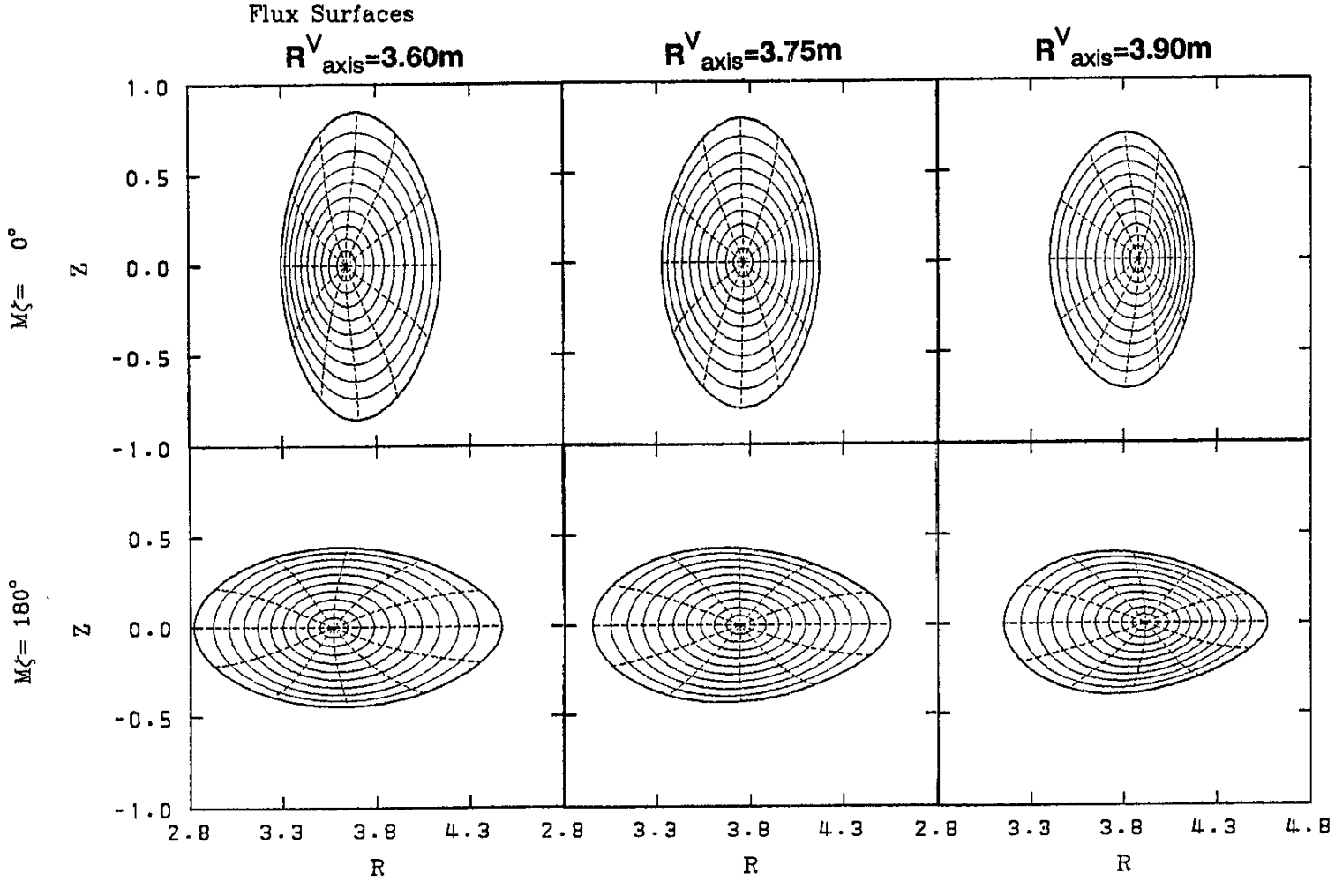
Flux Surfaces
R^V_axis=3.60m
R^V_axis=3.75m
R^V_axis=3.90m
Mζ= 0°
Mζ= 180°
Z
R
1.0
0.5
0.0
-0.5
-1.0
2.8
3.3
3.8
4.3
4.8

Fig.1(a)

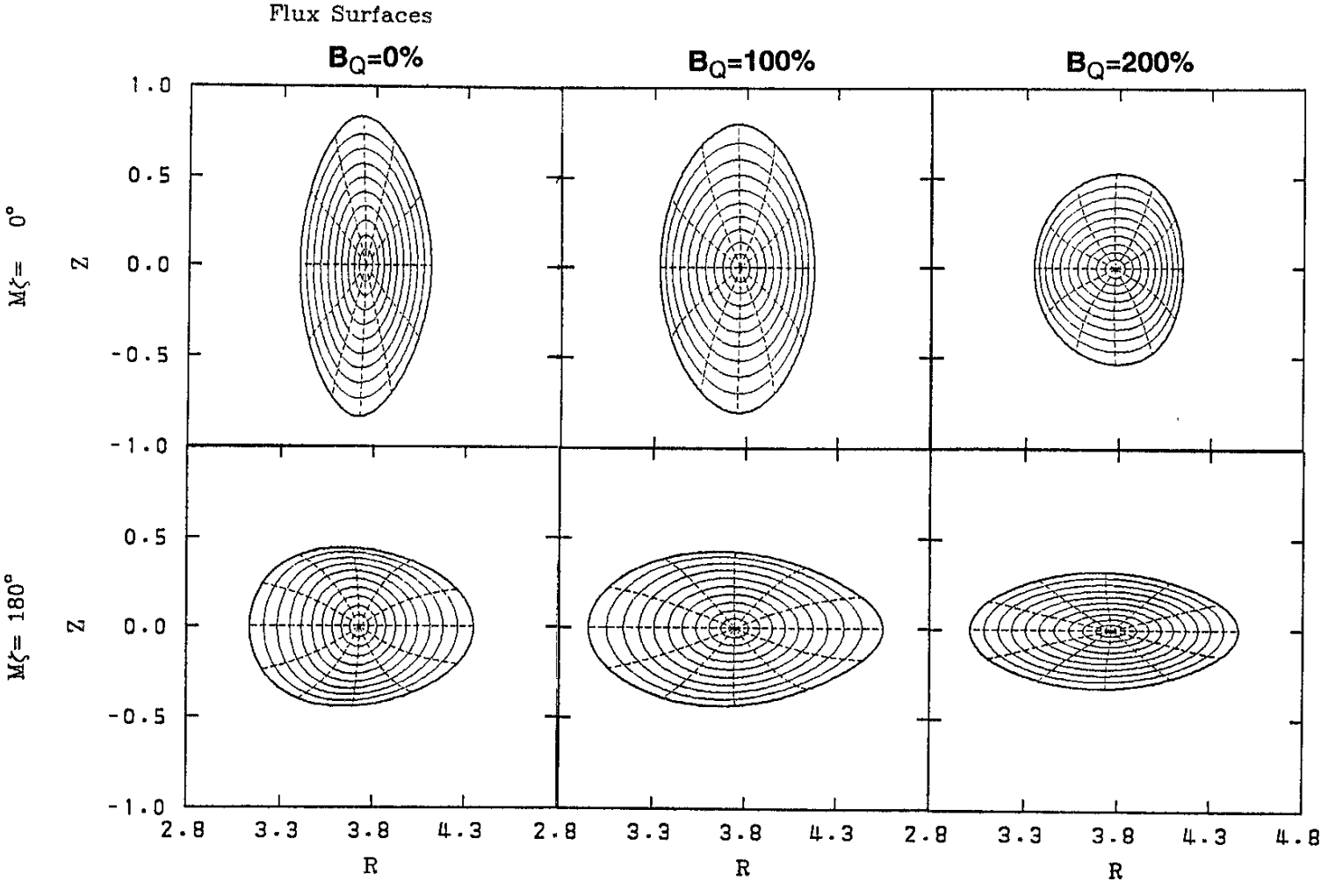
Flux Surfaces
B_Q=0%
B_Q=100%
B_Q=200%
Mζ= 0°
Mζ= 180°
Z
R
1.0
0.5
0.0
-0.5
-1.0
2.8
3.3
3.8
4.3
4.8

Fig.1(b)

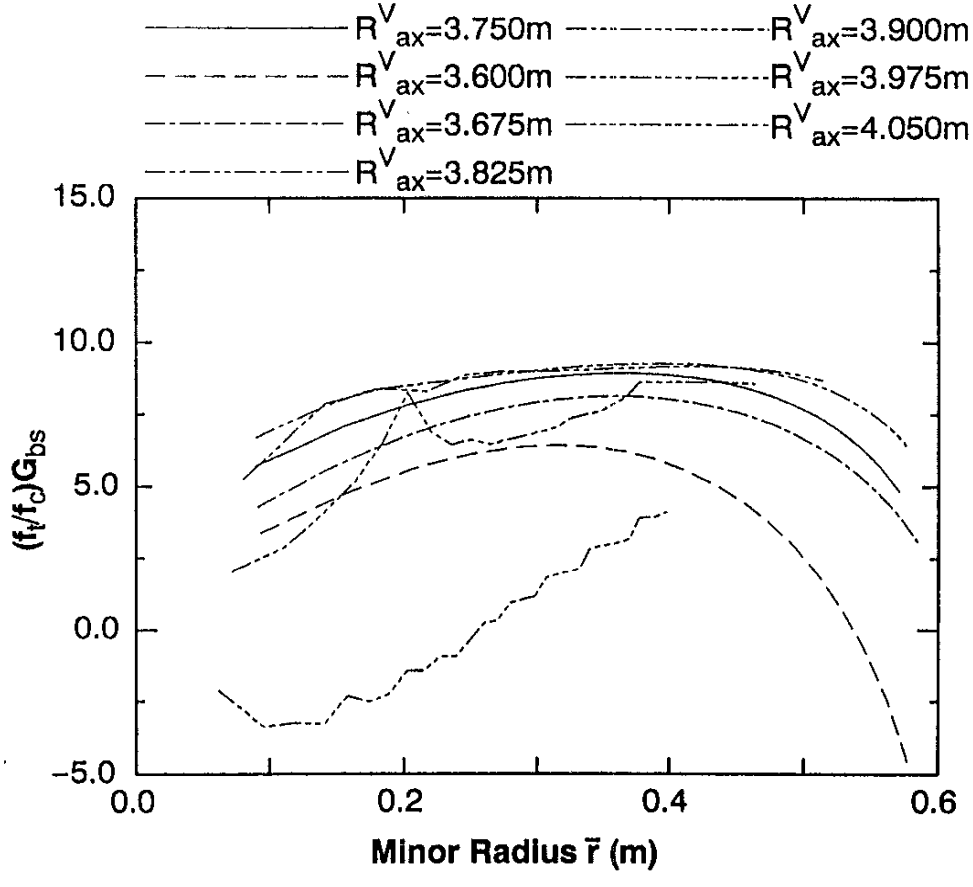
R^V_ax=3.750m
R^V_ax=3.600m
R^V_ax=3.675m
R^V_ax=3.825m
R^V_ax=3.900m
R^V_ax=3.975m
R^V_ax=4.050m
15.0
10.0
5.0
0.0
-5.0
0.0
0.2
0.4
0.6
(f_t/f_C)G_bs
Minor Radius r̄ (m)

Fig.2(a)

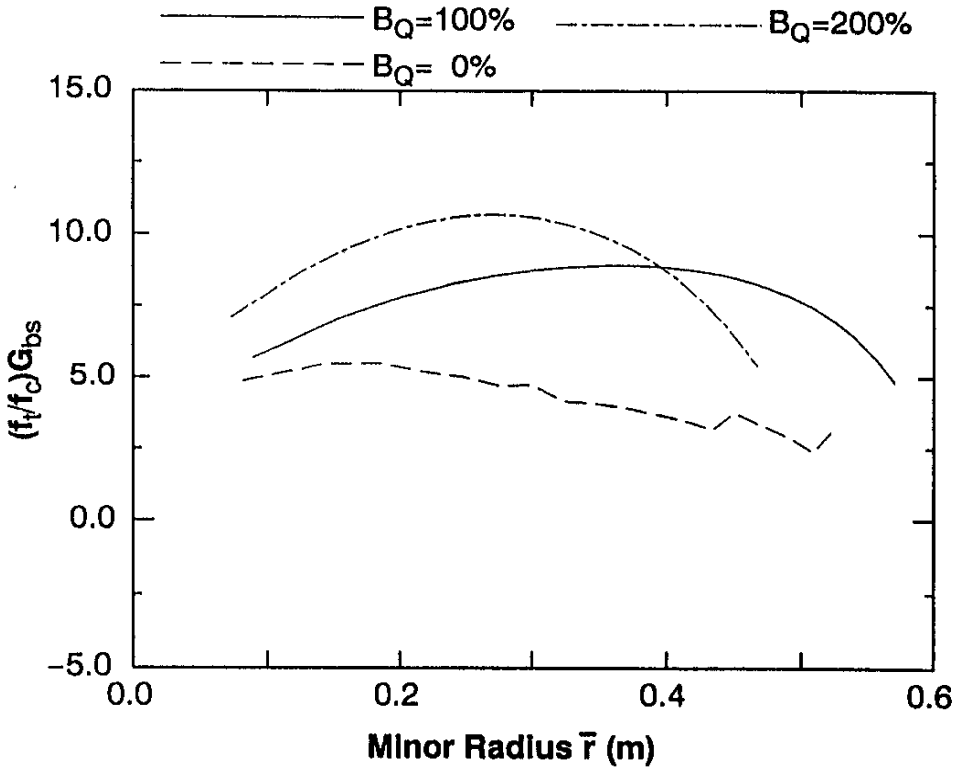
B_Q=100%
B_Q=200%
B_Q= 0%
15.0
10.0
5.0
0.0
-5.0
0.0
0.2
0.4
0.6
$(f_t/f_C)G_{bs}$
Minor Radius $\bar{r}$ (m)

Fig.2(b)

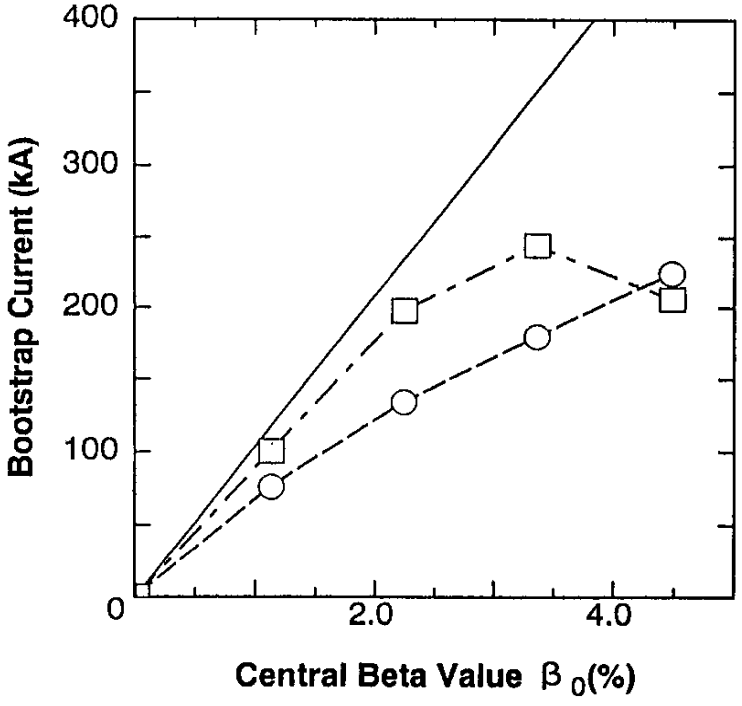
400
300
200
100
0
Bootstrap Current (kA)
2.0
4.0
Central Beta Value β 0(%)

Fig.3(a)

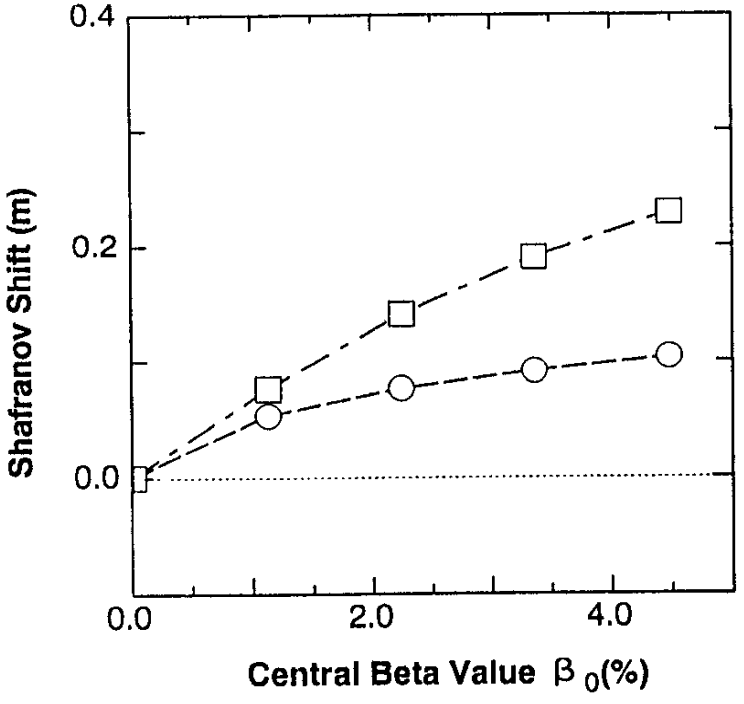
0.4
0.2
0.0
Shafranov Shift (m)
0.0
2.0
4.0
Central Beta Value β 0(%)

Fig.3(b)

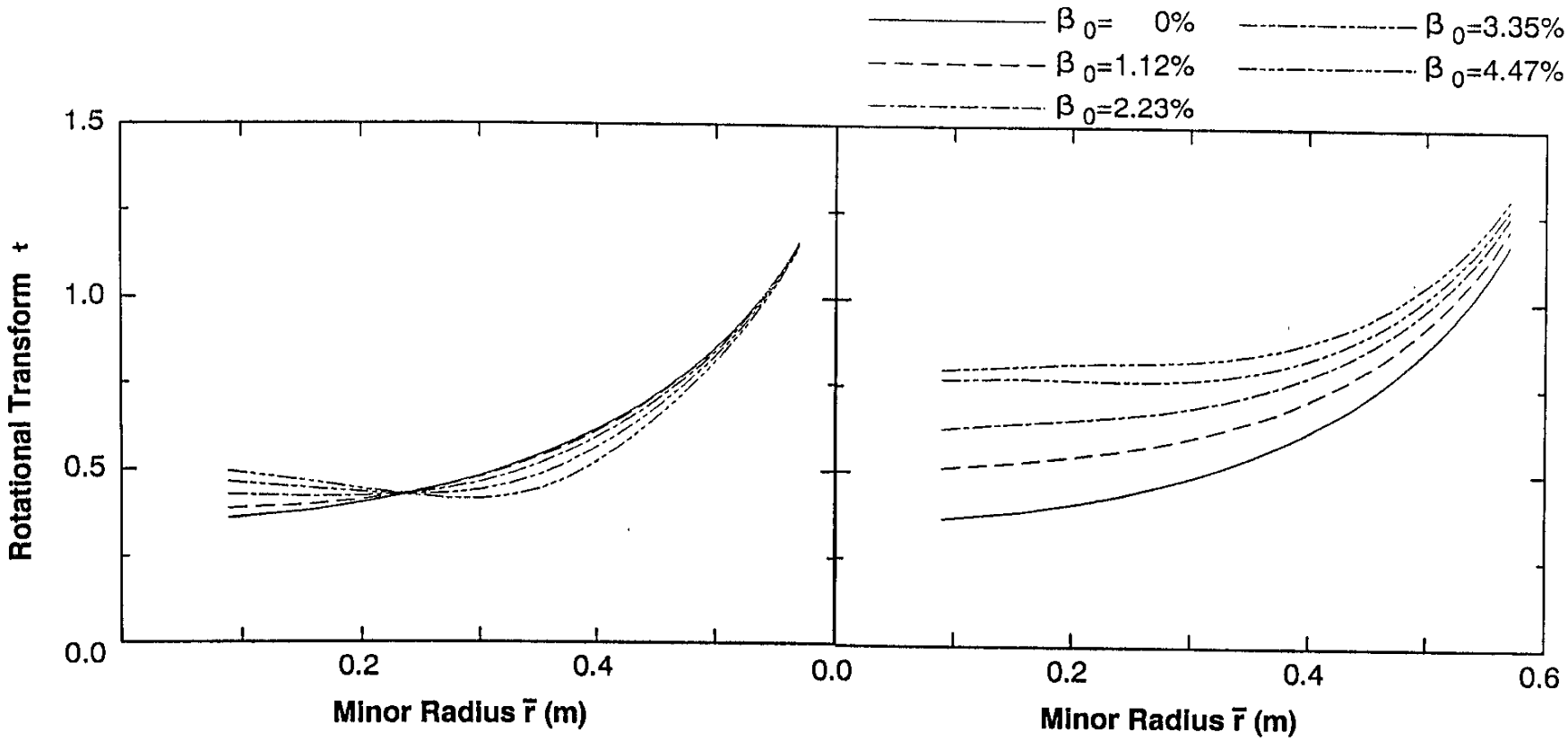
β 0= 0%
β 0=1.12%
β 0=2.23%
β 0=3.35%
β 0=4.47%
Rotational Transform ι
1.5
1.0
0.5
0.0
0.2
0.4
0.0
0.2
0.4
0.6
Minor Radius r̄ (m)
Minor Radius r̄ (m)

Fig.4

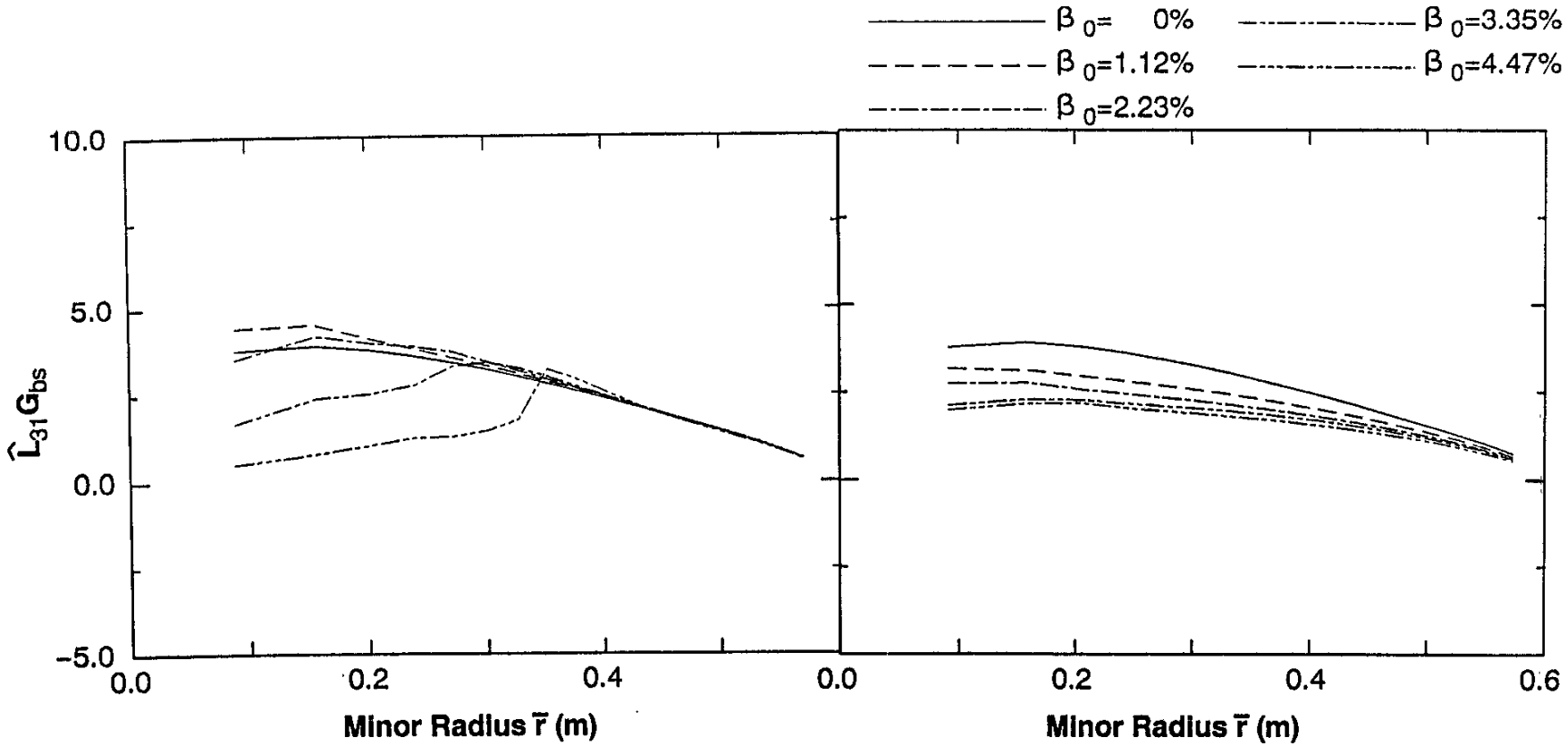
β 0= 0%
β 0=1.12%
β 0=2.23%
β 0=3.35%
β 0=4.47%
10.0
5.0
0.0
-5.0
$\hat{L}_{31}G_{bs}$
0.0
0.2
0.4
0.0
0.2
0.4
0.6
Minor Radius r̄ (m)
Minor Radius r̄ (m)

Fig.5

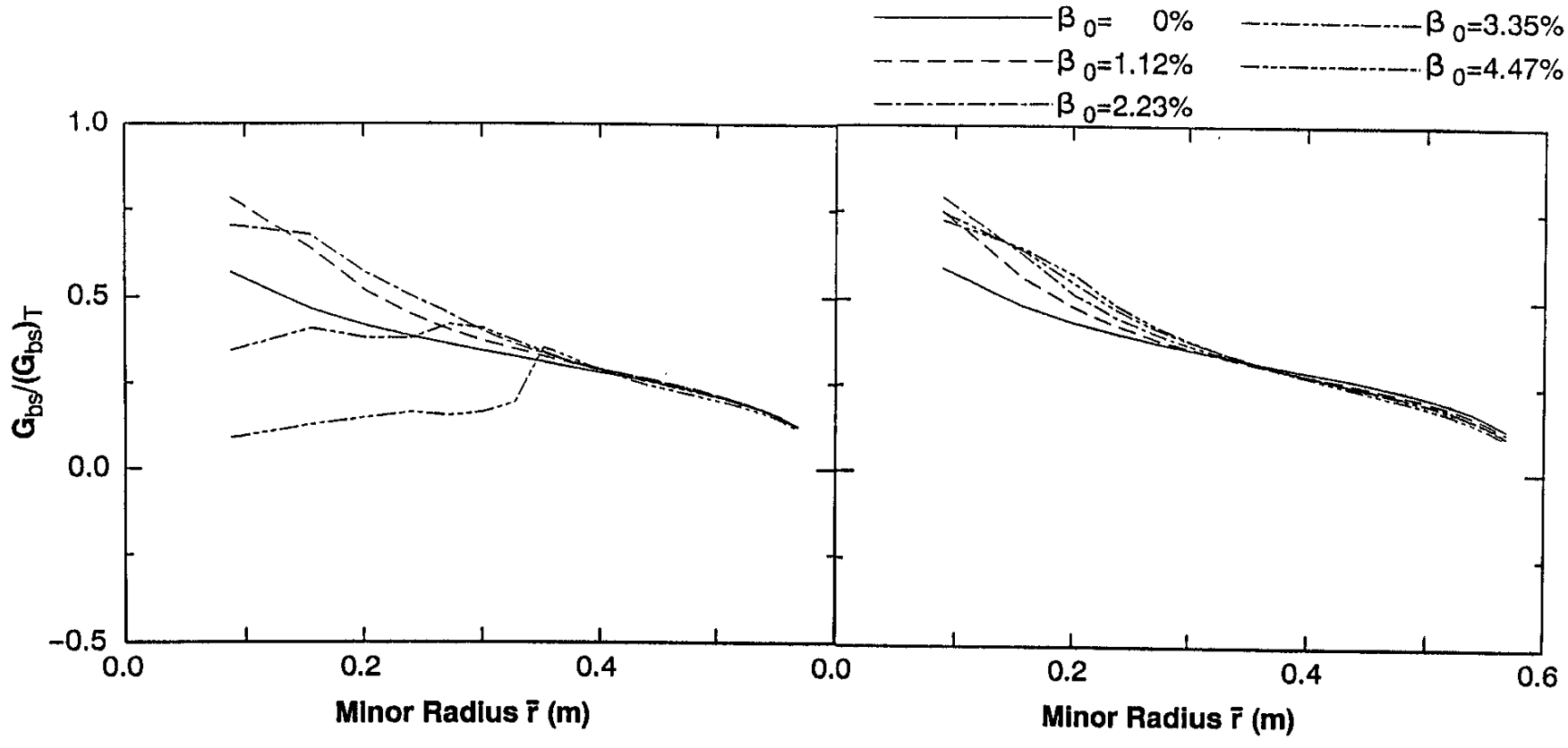
β 0= 0%
β 0=1.12%
β 0=2.23%
β 0=3.35%
β 0=4.47%
1.0
0.5
0.0
-0.5
$G_{bs}/(G_{bs})_T$
0.0
0.2
0.4
0.0
0.2
0.4
0.6
Minor Radius r̄ (m)
Minor Radius r̄ (m)

Fig.6

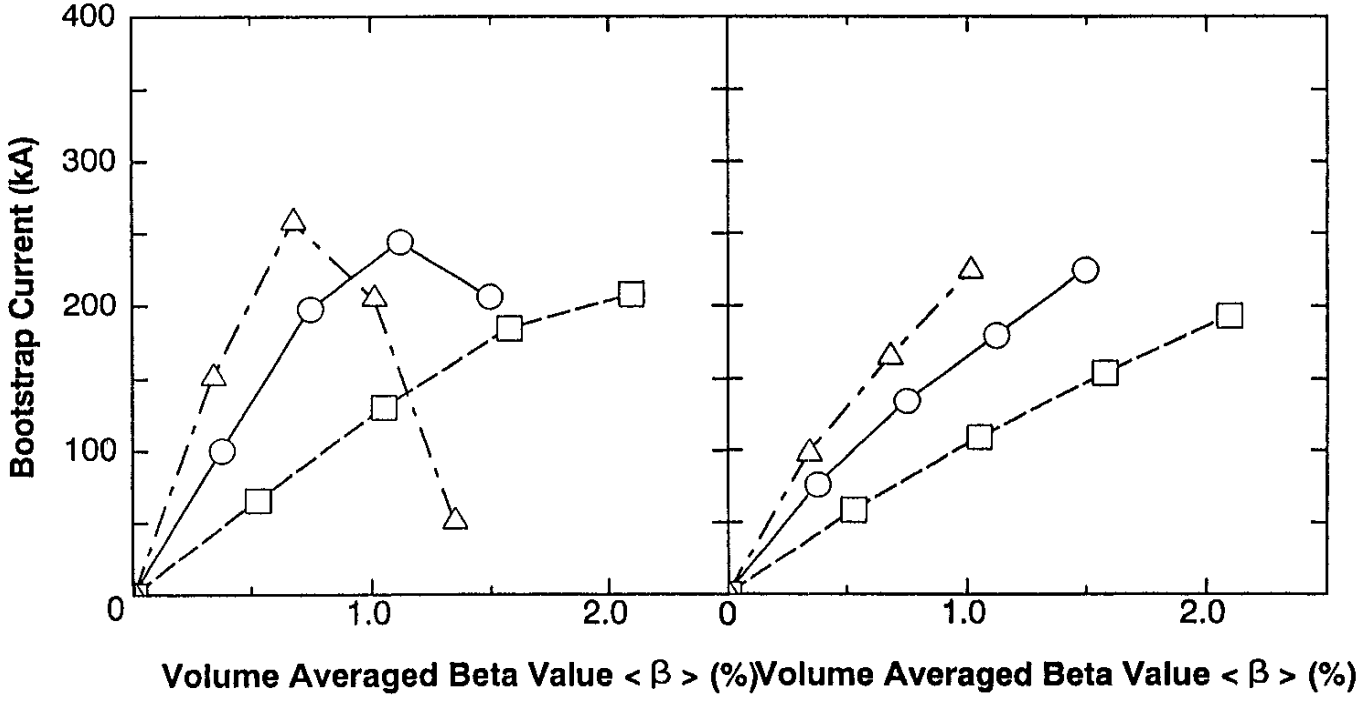
400
300
200
100
0
Bootstrap Current (kA)
1.0
2.0
0
1.0
2.0
Volume Averaged Beta Value < β > (%)Volume Averaged Beta Value < β > (%)

Fig.7

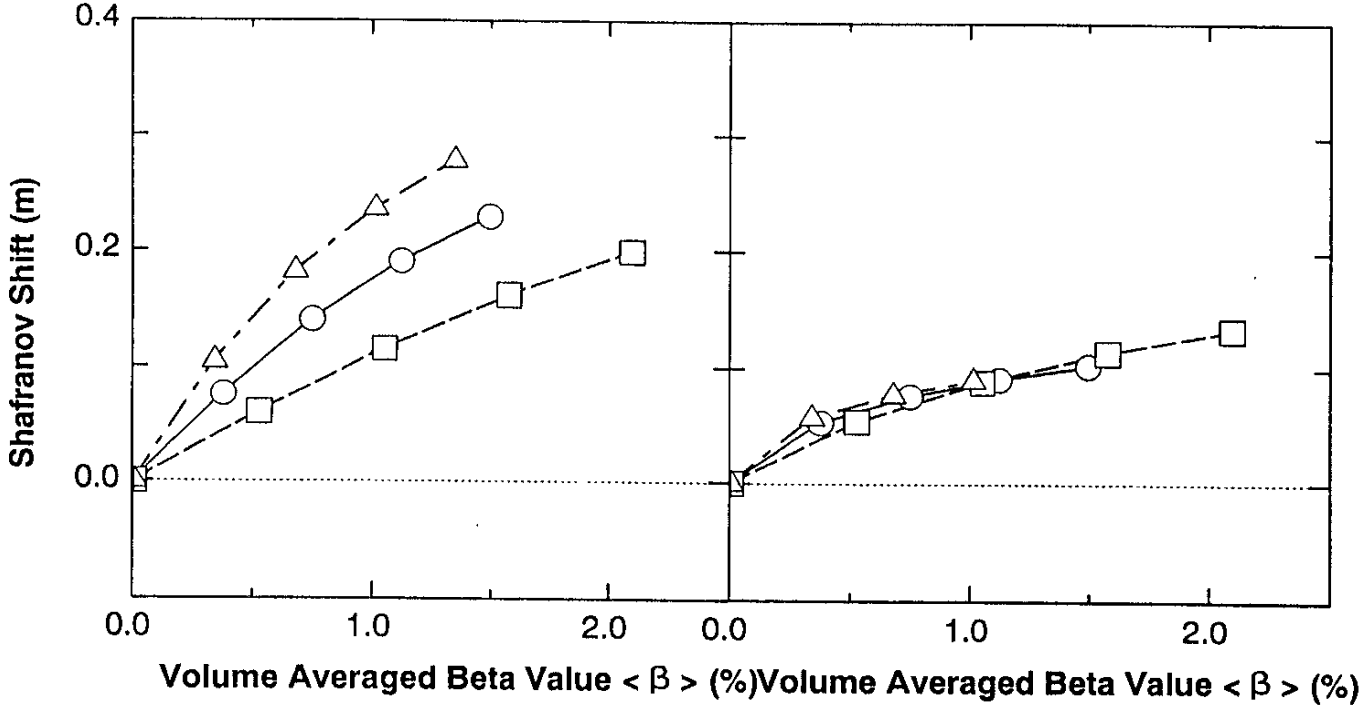
0.4
0.2
0.0
Shafranov Shift (m)
0.0
1.0
2.0
0.0
1.0
2.0
Volume Averaged Beta Value < β > (%)Volume Averaged Beta Value < β > (%)

Fig.8

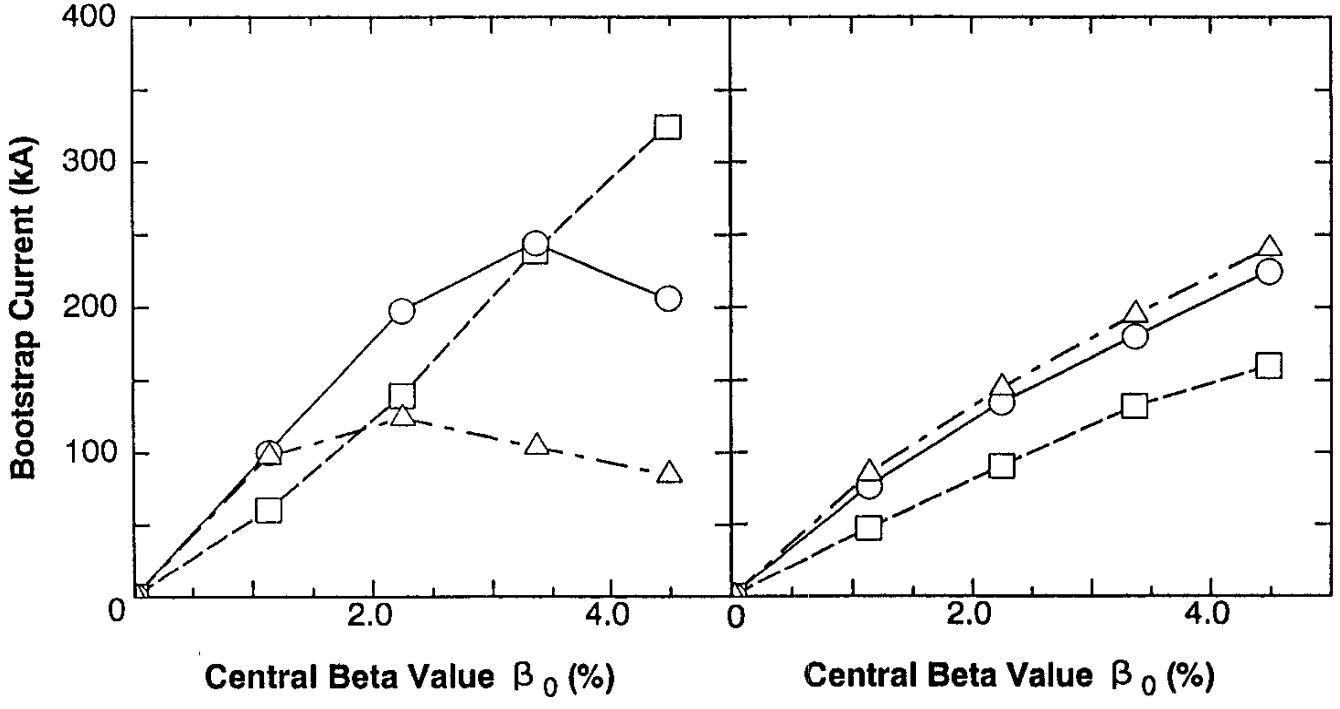
400
300
200
100
0
Bootstrap Current (kA)
2.0
4.0
Central Beta Value β_0 (%)
0
2.0
4.0
Central Beta Value β_0 (%)

Fig.9

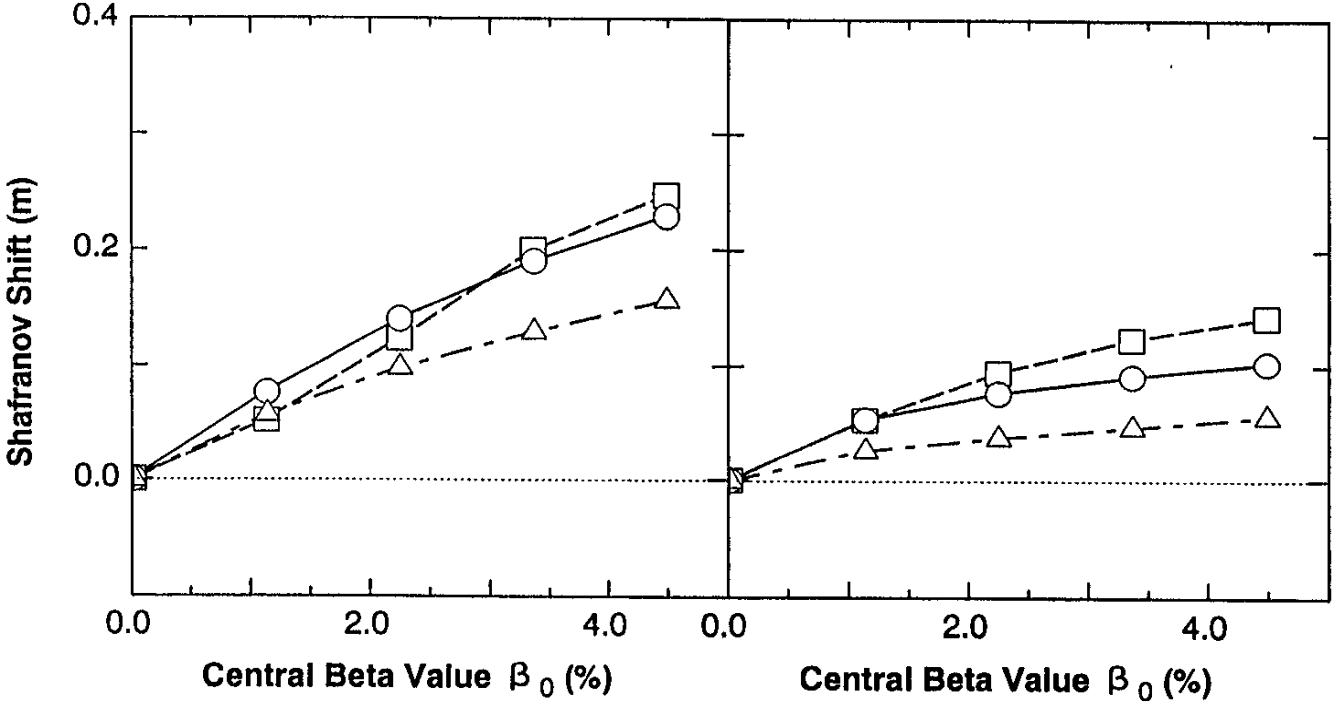
0.4
0.2
0.0
Shafranov Shift (m)
0.0
2.0
4.0
Central Beta Value β 0 (%)
0.0
2.0
4.0
Central Beta Value β 0 (%)

Fig.10

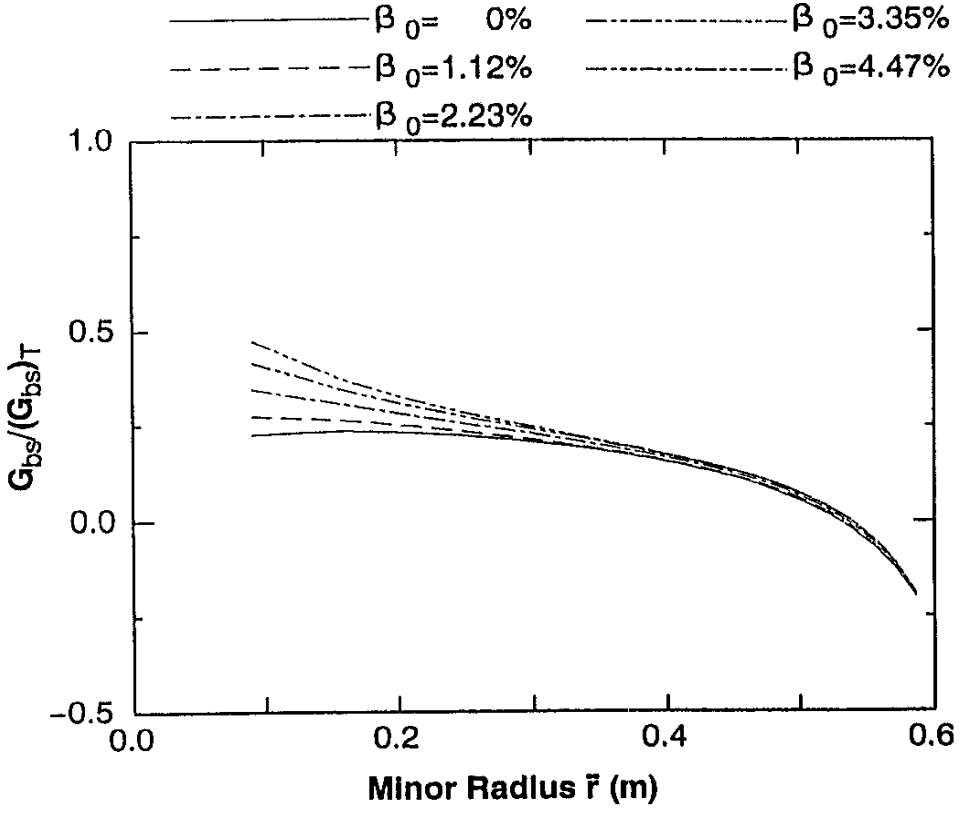
β 0= 0%
β 0=1.12%
β 0=2.23%
β 0=3.35%
β 0=4.47%
1.0
0.5
0.0
−0.5
0.0
0.2
0.4
0.6
$G_{bs}/(G_{bs})_T$
Minor Radius r̄ (m)

Fig.11(a)

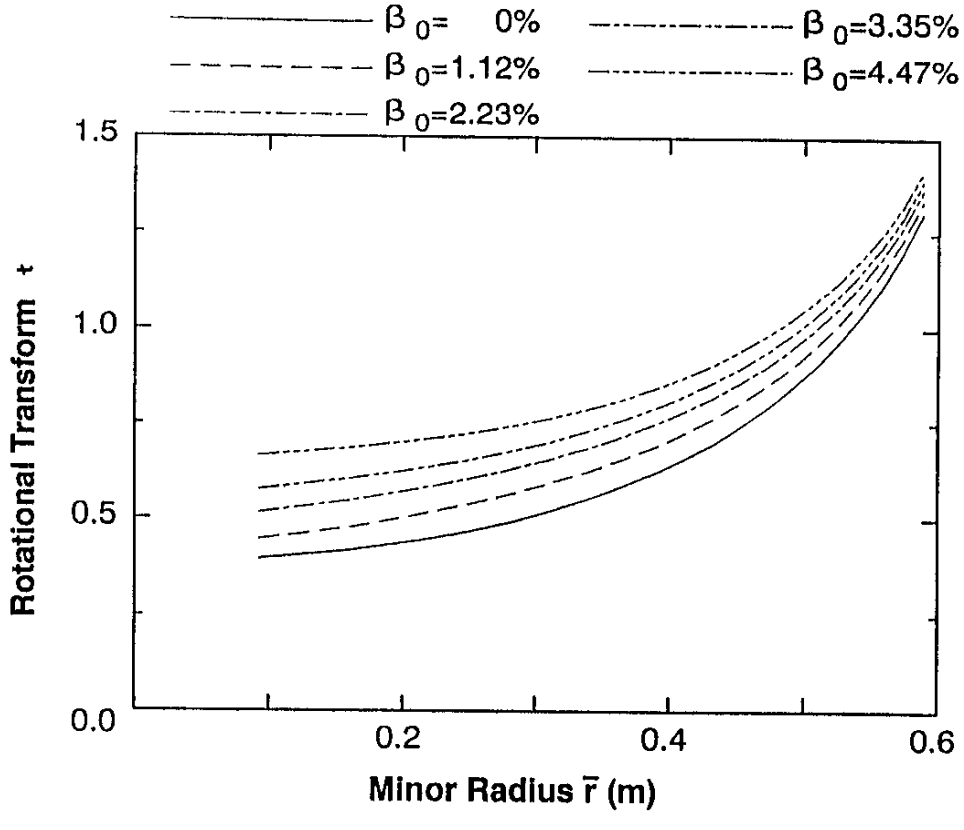
β 0= 0%
β 0=1.12%
β 0=2.23%
β 0=3.35%
β 0=4.47%
Rotational Transform ι
1.5
1.0
0.5
0.0
0.2
0.4
0.6
Minor Radius r̄ (m)

Fig.11(b)

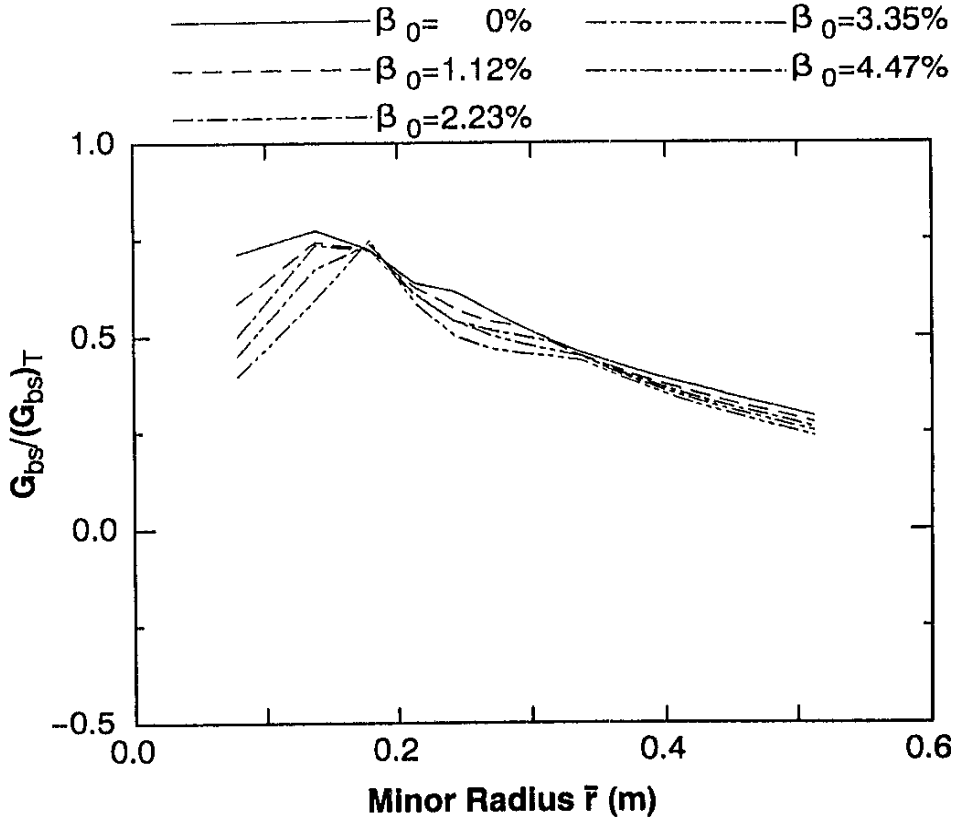
β 0= 0%
β 0=1.12%
β 0=2.23%
β 0=3.35%
β 0=4.47%
1.0
0.5
0.0
-0.5
0.0
0.2
0.4
0.6
G_bs/(G_bs)_T
Minor Radius r̄ (m)

Fig.12(a)

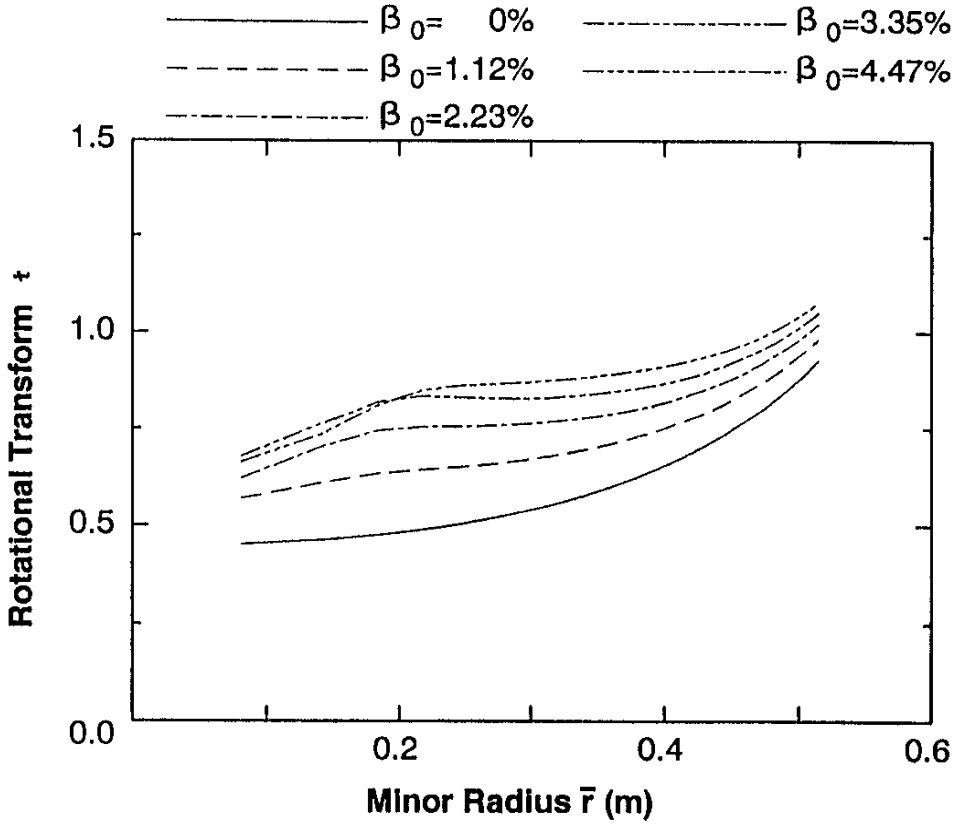
β 0= 0%
β 0=1.12%
β 0=2.23%
β 0=3.35%
β 0=4.47%
1.5
1.0
0.5
0.0
Rotational Transform ι
0.2
0.4
0.6
Minor Radius r̄ (m)

Fig.12(b)

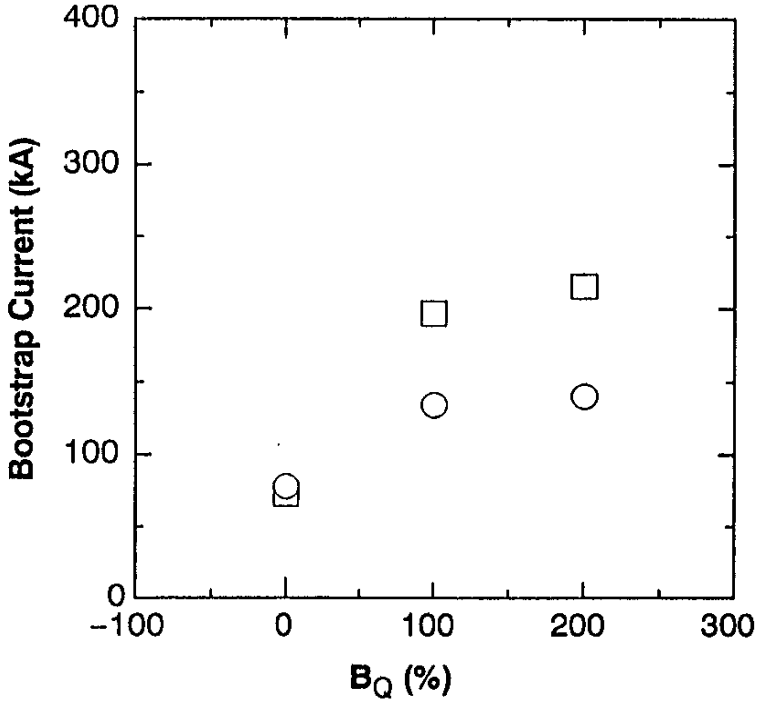

Fig.13(a)

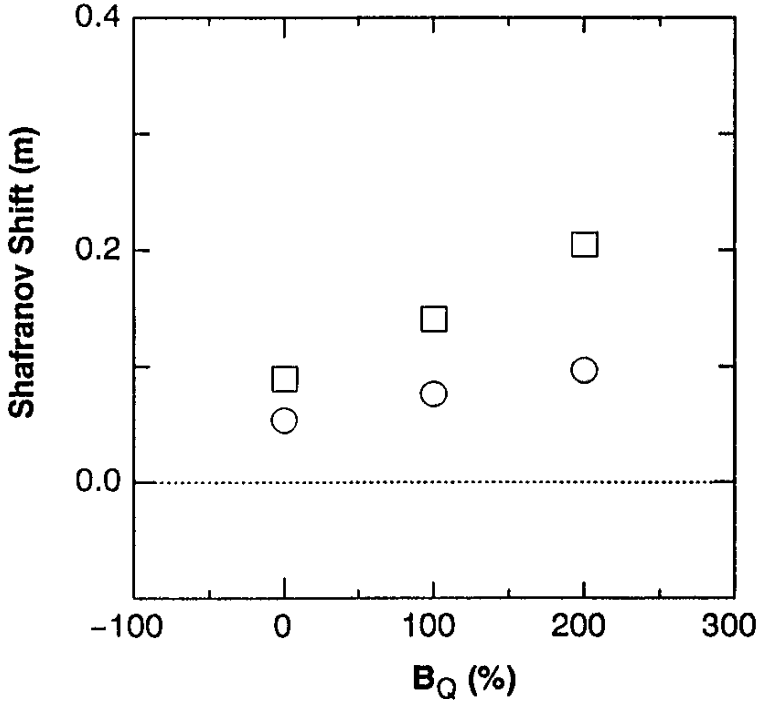

Fig.13(b)

Recent Issues of NIFS Series

NIFS-89 H. Sugama, N. Nakajima and M.Wakatani, *Nonlinear Behavior of Multiple-Helicity Resistive Interchange Modes near Marginally Stable States;* May 1991

NIFS-90 H. Hojo and T.Hatori, *Radial Transport Induced by Rotating RF Fields and Breakdown of Intrinsic Ambipolarity in a Magnetic Mirror;* May 1991

NIFS-91 M. Tanaka, S. Murakami, H. Takamaru and T.Sato, *Macroscale Implicit, Electromagnetic Particle Simulation of Inhomogeneous and Magnetized Plasmas in Multi-Dimensions;* May 1991

NIFS-92 S. - I. Itoh, *H-mode Physics, -Experimental Observations and Model Theories-, Lecture Notes, Spring College on Plasma Physics, May 27 - June 21 1991 at International Centre for Theoretical Physics (IAEA UNESCO) Trieste, Italy ;* Jun. 1991

NIFS-93 Y. Miura, K. Itoh, S. - I. Itoh, T. Takizuka, H. Tamai, T. Matsuda, N. Suzuki, M. Mori, H. Maeda and O. Kardaun, *Geometric Dependence of the Scaling Law on the Energy Confinement Time in H-mode Discharges;* Jun. 1991

NIFS-94 H. Sanuki, K. Itoh, K. Ida and S. - I. Itoh, *On Radial Electric Field Structure in CHS Torsatron / Heliotron;* Jun. 1991

NIFS-95 K. Itoh, H. Sanuki and S. - I. Itoh, *Influence of Fast Ion Loss on Radial Electric Field in Wendelstein VII-A Stellarator;* Jun. 1991

NIFS-96 S. - I. Itoh, K. Itoh, A. Fukuyama, *ELMy-H mode as Limit Cycle and Chaotic Oscillations in Tokamak Plasmas;* Jun. 1991

NIFS-97 K. Itoh, S. - I. Itoh, H. Sanuki, A. Fukuyama, *An H-mode-Like Bifurcation in Core Plasma of Stellarators;* Jun. 1991

NIFS-98 H. Hojo, T. Watanabe, M. Inutake, M. Ichimura and S. Miyoshi, *Axial Pressure Profile Effects on Flute Interchange Stability in the Tandem Mirror GAMMA 10;* Jun. 1991

NIFS-99 A. Usadi, A. Kageyama, K. Watanabe and T. Sato, *A Global Simulation of the Magnetosphere with a Long Tail : Southward and Northward IMF;* Jun. 1991

NIFS-100 H. Hojo, T. Ogawa and M. Kono, *Fluid Description of Ponderomotive Force Compatible with the Kinetic One in a Warm Plasma* ; July

1991

NIFS-101 H. Momota, A. Ishida, Y. Kohzaki, G. H. Miley, S. Ohi, M. Ohnishi K. Yoshikawa, K. Sato, L. C. Steinhauer, Y. Tomita and M. Tuszewski *Conceptual Design of D-^{3}He FRC Reactor "ARTEMIS"* ; July 1991

NIFS-102 N. Nakajima and M. Okamoto, *Rotations of Bulk Ions and Impurities in Non-Axisymmetric Toroidal Systems* ; July 1991

NIFS-103 A. J. Lichtenberg, K. Itoh, S. - I. Itoh and A. Fukuyama, *The Role of Stochasticity in Sawtooth Oscillation* ; Aug. 1991

NIFS-104 K. Yamazaki and T. Amano, *Plasma Transport Simulation Modeling for Helical Confinement Systems;* Aug. 1991

NIFS-105 T. Sato, T. Hayashi, K. Watanabe, R. Horiuchi, M. Tanaka, N. Sawairi and K. Kusano, *Role of Compressibility on Driven Magnetic Reconnection ;* Aug. 1991

NIFS-106 Qian Wen - Jia, Duan Yun - Bo, Wang Rong - Long and H. Narumi, *Electron Impact Excitation of Positive Ions - Partial Wave Approach in Coulomb - Eikonal Approximation* ; Sep. 1991

NIFS-107 S. Murakami and T. Sato, *Macroscale Particle Simulation of Externally Driven Magnetic Reconnection;* Sep. 1991

NIFS-108 Y. Ogawa, T. Amano, N. Nakajima, Y. Ohyabu, K. Yamazaki, S. P. Hirshman, W. I. van Rij and K. C. Shaing, *Neoclassical Transport Analysis in the Banana Regime on Large Helical Device (LHD) with the DKES Code;* Sep. 1991

NIFS-109 Y. Kondoh, *Thought Analysis on Relaxation and General Principle to Find Relaxed State;* Sep. 1991

NIFS-110 H. Yamada, K. Ida, H. Iguchi, K. Hanatani, S. Morita, O. Kaneko, H. C. Howe, S. P. Hirshman, D. K. Lee, H. Arimoto, M. Hosokawa, H. Idei, S. Kubo, K. Matsuoka, K. Nishimura, S. Okamura, Y. Takeiri, Y. Takita and C. Takahashi, *Shafranov Shift in Low-Aspect-Ratio Heliotron / Torsatron CHS* ; Sep 1991

NIFS-111 R. Horiuchi, M. Uchida and T. Sato, *Simulation Study of Stepwise Relaxation in a Spheromak Plasma ;* Oct. 1991

NIFS-112 M. Sasao, Y. Okabe, A. Fujisawa, H. Iguchi, J. Fujita, H. Yamaoka and M. Wada, *Development of Negative Heavy Ion Sources for Plasma Potential Measurement* ; Oct. 1991

NIFS-113 S. Kawata and H. Nakashima, *Tritium Content of a DT Pellet in Inertial Confinement Fusion* ; Oct. 1991

NIFS-114 M. Okamoto, N. Nakajima and H. Sugama, *Plasma Parameter Estimations for the Large Helical Device Based on the Gyro-Reduced Bohm Scaling* ; Oct. 1991

NIFS-115 Y. Okabe, *Study of Au^- Production in a Plasma-Sputter Type Negative Ion Source* ; Oct. 1991

NIFS-116 M. Sakamoto, K. N. Sato, Y. Ogawa, K. Kawahata, S. Hirokura, S. Okajima, K. Adati, Y. Hamada, S. Hidekuma, K. Ida, Y. Kawasumi, M. Kojima, K. Masai, S. Morita, H. Takahashi, Y. Taniguchi, K. Toi and T. Tsuzuki, *Fast Cooling Phenomena with Ice Pellet Injection in the JIPP T-IIU Tokamak;* Oct. 1991

NIFS-117 K. Itoh, H. Sanuki and S. -I. Itoh, *Fast Ion Loss and Radial Electric Field in Wendelstein VII-Λ Stellarator*; Oct. 1991

NIFS-118 Y. Kondoh and Y. Hosaka, *Kernel Optimum Nearly-analytical Discretization (KOND) Method Applied to Parabolic Equations <<KOND-P Scheme>>;* Nov. 1991

NIFS-119 T. Yabe and T. Ishikawa, *Two- and Three-Dimensional Simulation Code for Radiation-Hydrodynamics in ICF*; Nov. 1991

NIFS-120 S. Kawata, M. Shiromoto and T. Teramoto, *Density-Carrying Particle Method for Fluid* ; Nov. 1991

NIFS-121 T. Ishikawa, P. Y. Wang, K. Wakui and T. Yabe, *A Method for the High-speed Generation of Random Numbers with Arbitrary Distributions;* Nov. 1991

NIFS-122 K. Yamazaki, H. Kaneko, Y. Taniguchi, O. Motojima and LHD Design Group, *Status of LHD Control System Design ; Dec. 1991*

NIFS-123 Y. Kondoh, *Relaxed State of Energy in Incompressible Fluid and Incompressible MHD Fluid* ; Dec. 1991

NIFS-124 K. Ida, S. Hidekuma, M. Kojima, Y. Miura, S. Tsuji, K. Hoshino, M. Mori, N. Suzuki, T. Yamauchi and JFT-2M Group, *Edge Poloidal Rotation Profiles of H-Mode Plasmas in the JFT-2M Tokamak ;* Dec. 1991

NIFS-125 H. Sugama and M. Wakatani, *Statistical Analysis of Anomalous Transport in Resistive Interchange Turbulence* ;Dec. 1991

NIFS-126 K. Narihara, *A Steady State Tokamak Operation by Use of Magnetic Monopoles* ; Dec. 1991

NIFS-127 K. Itoh, S. -I. Itoh and A. Fukuyama, *Energy Transport in the Steady State Plasma Sustained by DC Helicity Current Drive* ;Jan. 1992

NIFS-128 Y. Hamada, Y. Kawasumi, K. Masai, H. Iguchi, A. Fujisawa, JIPP T-IIU Group and Y. Abe, *New Hight Voltage Parallel Plate Analyzer* ; Jan. 1992

NIFS-129 K. Ida and T. Kato, *Line-Emission Cross Sections for the Charge-exchange Reaction between Fully Stripped Carbon and Atomic Hydrogen in Tokamak Plasma*; Jan. 1992

NIFS-130 T. Hayashi, A. Takei and T. Sato, *Magnetic Surface Breaking in 3D MHD Equilibria of l=2 Heliotron* ; Jan. 1992

NIFS-131 K. Itoh, K. Iguchi and S. -I. Itoh, *Beta Limit of Resistive Plasma in Torsatron/Heliotron* ; Feb. 1992

NIFS-132 K. Sato and F. Miyawaki, *Formation of Presheath and Current-Free Double Layer in a Two-Electron-Temperture Plasma* ; Feb. 1992

NIFS-133 T. Maruyama and S. Kawata, *Superposed-Laser Electron Acceleration* Feb. 1992

NIFS-134 Y. Miura, F. Okano, N. Suzuki, M. Mori, K. Hoshino, H. Maeda, T. Takizuka, JFT-2M Group, S.-I. Itoh and K. Itoh, *Rapid Change of Hydrogen Neutral Energy Distribution at L/H-Transition in JFT-2M H-mode ;* Feb. 1992

NIFS-135 H. Ji, H. Toyama, A. Fujisawa, S. Shinohara and K. Miyamoto *Fluctuation and Edge Current Sustainment in a Reversed-Field-Pinch;* Feb. 1992

NIFS-136 K. Sato and F. Miyawaki, *Heat Flow of a Two-Electron-Temperature Plasma through the Sheath in the Presence of Electron Emission;* Mar. 1992

NIFS-137 T. Hayashi, U. Schwenn and E. Strumberger, *Field Line Diversion Properties of Finite β Helias Equilibria;* Mar. 1992

NIFS-138 T. Yamagishi, *Kinetic Approach to Long Wave Length Modes in Rotating Plasmas*; Mar. 1992